Technical Report Documentation Page

1. Report No.	2. Government Accession No.	3. Recipient's Catalog No.
eScholarship UC item 761269mb		

4. Title and Subtitle	5. Report Date
Impact of Takeoff Trajectory Design on Performance and Noise for Advanced Air Mobility Aircraft	December 2025
	6. Performing Organization Code

7. Author(s)	8. Performing Organization Report No.
Gonzalez, V., Yeung, S., Huynh, J., & Hansman, R. J.	

9. Performing Organization Name and Address	10. Work Unit No. (TRAIS)
Center of Excellence for: Alternative Jet Fuels and Environment Massachusetts Institute of Technology, 77 Massachusetts Ave., Cambridge, MA, 02139, USA	11. Contract or Grant No. 13-C-AJFE-MIT-112, 131

12. Sponsoring Agency Name and Address	13. Type of Report and Period Covered
Federal Aviation Administration Office of Environment and Energy	Journal Article
	14. Sponsoring Agency Code

15. Supplementary Notes

https://escholarship.org/uc/item/761269mb

16. Abstract

A broad range of AAM aircraft are currently in development, each with varying community noise footprints and energy consumption depending on the specifics of their departure and arrival flight trajectories, which must be understood for effective airspace integration. This work presents a framework for analyzing AAM trajectory design, focusing on key performance characteristics including community noise impact, energy consumption, and flight duration. The framework can be applied to diverse AAM vehicle types, as demonstrated in this work on a Blown-Flap Short Takeoff and Landing vehicle, a Tilt-Rotor Vertical Takeoff and Landing vehicle, and a Lift plus Cruise Vertical Takeoff and Landing vehicle. Results of comparing various takeoff procedures for each vehicle show trade-offs between community noise, energy consumption, and flight duration, highlighting the importance of strategic trajectory design.

17. Key Words	18. Distribution Statement
Flight Trajectory, Aircrafts, Advanced Air Mobility, Multi Rotor, Flight Control Surfaces, Vertical Takeoff and Landing, Energy Consumption, Spacecraft Design, Short Takeoff and Landing, Airspace, ASCENT	

19. Security Classif. (of this report)	20. Security Classif. (of this page)	21. No. of Pages	22. Price
Unclassified	Unclassified		

Impact of Takeoff Trajectory Design on Performance and Noise for AAM Aircraft

Victoria Gonzalez*, Seraphin Yeung†, and Jacqueline Huynh‡
University of California Irvine, 4200 Engineering Gateway, Irvine, CA, 92617, USA

R. John Hansman§
Massachusetts Institute of Technology, 77 Massachusetts Ave., Cambridge, MA, 02139, USA

A broad range of AAM aircraft are currently in development, each with varying community noise footprints and energy consumption depending on the specifics of their departure and arrival flight trajectories, which must be understood for effective airspace integration. This work presents a framework for analyzing AAM trajectory design, focusing on key performance characteristics including community noise impact, energy consumption, and flight duration. The framework can be applied to diverse AAM vehicle types, as demonstrated in this work on a Blown-Flap Short Takeoff and Landing vehicle, a Tilt-Rotor Vertical Takeoff and Landing vehicle, and a Lift plus Cruise Vertical Takeoff and Landing vehicle. Results of comparing various takeoff procedures for each vehicle show trade-offs between community noise, energy consumption, and flight duration, highlighting the importance of strategic trajectory design.

I. Nomenclature

a	=	acceleration
AAM	=	Advanced Air Mobility
ABEAT	=	ANOPP2 Blade Element Acoustic Tool
AEDT	=	FAA Aviation Environmental Design Tool
ANOPP	=	NASA Aircraft NOise Prediction Program
ATM	=	Air Traffic Management
dBA	=	decibels A-weighted
deg	=	Degrees

*Graduate Student, Department of Mechanical and Aerospace Engineering, AIAA Student Member, Corresponding Author, vpelleri@uci.edu
†Graduate Student, Department of Mechanical and Aerospace Engineering, AIAA Student Member
‡Assistant Professor, Department of Mechanical and Aerospace Engineering, AIAA Senior Member
§Professor, Department of Aeronautics and Astronautics, AIAA Fellow.
Presented as Paper 2024-4076 Impact of Flight Trajectory Design on Performance and Noise for AAM Aircraft at the AIAA Aviation 2024 Forum, Las Vegas, NV, July 31, 2024

eSTOL	=	Electric Short Takeoff and Landing
eVTOL	=	Electric Vertical Takeoff and Landing
FAA	=	Federal Aviation Administration
ft	=	Feet
h	=	Acceleration altitude
kts	=	Knots
kWh	=	Kilowatt hours
$L_{A,Max}$	=	Maximum A-weighted Sound Pressure Level
lbs	=	Pound force
LPC	=	Lift Plus Cruise
m	=	Mass
MPPI	=	Model Predictive Path Integral
NAS	=	National Airspace System
NDARC	=	NASA Design and Analysis of Rotorcraft
nm	=	Nautical miles
N_R	=	Number of rotors
R	=	Rotor diameter
RPM	=	Revolutions per Minute
RVLT	=	NASA Revolutionary Vertical Lift Technology
s	=	Seconds
SEL	=	Sound Exposure Level
T	=	Total thrust force per rotor
V_1	=	Velocity where wing lift is 50% aircraft weight
V_j	=	Jet Velocity
V_∞	=	Free stream velocity
X	=	Aircraft state vector
$()_C$	=	Cruise-direction
$()_L$	=	Lift-direction
$()_x$	=	x-direction
$()_z$	=	z-direction
α	=	Angle of attack
$\Delta\theta_B$	=	Change in blade root pitch

δ_f = Flap detent

γ = Flight path angle

γ_c = Flight path angle of climb segments

γ_i = Flight path angle of initial climb for eSTOL flights

γ_t = Flight path angle of transition for eVTOL flights

τ = Rotor tilt angle

II. Introduction

As large cities see constant increases in urbanization and traffic congestion, Advanced Air Mobility (AAM) is proposed to combat inner and intra-city transportation challenges by leveraging the significant advancements in necessary technology of recent decades [1, 2]. This evolving concept for air transportation has a primary goal of providing scheduled and on-demand services as a part of inter-modal transportation links within major cities [1–4]. Such procedures are expected to operate at higher densities, lower altitudes, and in closer proximity to urban areas than legacy transport aircraft operations of the National Airspace System (NAS) today [1, 3]. As an emerging system entering the NAS, which has been evolving for decades, the introduction of AAM will require adherence to current regulations and procedures without disrupting existing air traffic procedures. Additionally, there are many distinct AAM aircraft being developed throughout the industry, all designed to meet diverse operation objectives and performance capabilities [5–7]. Thus, a diverse set of aircraft are intended to operate within a confined, densely populated airspace at low altitudes. However, the range of feasible procedures for the various AAM aircraft is not well understood and there is a lack of comprehensive comparative analysis. Furthermore, operations occurring at low altitude and within congested airspace present a dual emphasis on minimizing community noise impact and maximizing operational efficiency.

As Advanced Air Mobility continues to evolve and integrate into existing airspace systems, policymakers, regulators, and industry stakeholders must navigate diverse operational requirements and unique airspace constraints [8]. The challenge is to ensure safety, fairness, airspace efficiency, minimal power consumption and community noise impact. Understanding the impacts of substantial non-uniformity in vehicle design and performance on AAM traffic flow management is crucial for addressing these challenges. Therefore, the ability to reliably model aircraft performance and trajectories will play a crucial role in advancing the broader AAM ecosystem, emphasizing that ongoing progress in this area is vital [9]. To this end, several works have examined methods to assess flight performance for different AAM flight missions [9, 10], including acoustic aware path planning for a single aircraft [11, 12].Various tools have been developed that evaluate mission performance as a part of the AAM vehicle design process [13–15]. The geometric programming vehicle optimization method for optimizing cost per trip in [14] implemented a semi-emperical post-processing method for analyzing noise and found a general trend that higher lift-to-drag ratios and disk loading presented lower operating

costs, but were generally louder. Ackerman et al. [16] developed an acoustic constraint function for spatial path planning within a multi-vehicle trajectory generation framework. They, however, used simplified dynamic assumptions that do not consider specifics of vehicle performance capabilities.

Performance modeling for AAM aircraft is challenging due to limited vehicle data from proprietary markets. Concequently, NASA Revolutionary Vertical Lift Technology (RVLT) project designed six conceptual AAM vehicle designs using NASA's Design and Analysis of Rotorcraft (NDARC) software [17, 18]. NDARC is a rotorcraft design toolthat sizes a rotorcraft to meet specified flight conditions of an assumed mission and estimates the design's performance and is not directly capable of defining feasible missions of a provided rotorcraft [17, 19]. Hartman et al. [9] developed flight performance models for three of the NASA conceptual AAM designs [18], and leveraged NDARC to compute performance at operating conditions, but noted limitations in applicability to other AAM vehicles. Additionally, SUAVE [20], an open-source design and analysis tool, was compared with NDARC using the Kitty Hawk Cora eVTOL configuration, evaluating sensitivities through trade studies [21]. Clark and Alonso [15] applied SUAVE for designing AAM vehicles, analyzing performance, and modeling community noise impact using a medium-fidelity, semi-empirical approach, omitting broadband noise.

Public acceptance has been identified as one of the most limiting factors for successful implementation of large-scale AAM operations [22, 23]. Beyond ensuring the safety and affordability of the service for the end-user, public acceptance encompasses considerations regarding its impact on ground observers, including both visual and acoustic pollution [14, 22, 24–27]. While conventional aircraft noise modeling methods exist [28], they may not be compatible for modeling the unique noise sources of AAM aircraft. Detailed modeling, particularly for open-rotor noise is computationally expensive, leading many existing studies to make simplifying assumptions. For example, [14] and [27] use a semi-empirical expression to model the rotor and rotor vortex noise. Other works have developed methodologies that allow the conceptual design and modeling of multi-rotor aircraft, as well as evaluation based on their performance and community noise impacts. These studies use physics-based models [15, 29] to design low to medium-fidelity flight mission profiles based on unique vehicle capabilities and perform component-based noise evaluation. Emphasis is placed on the unique flight capabilities of conceptual AAM vehicles, where [30, 31] add on adapting tools and methodologies to better capture and characterize their noise profiles. Due to the sensitivity of noise around public acceptance for AAM vehicles, there has been little published results on noise modeling for AAM aircraft currently being developed in industry. For example, in [32] new flight procedures were evaluated using high-fidelity simulations; however, community noise results were not presented. Several papers also have made efforts to expand noise modeling capabilities of tools such as the FAA's Aviation Environmental Design Tool (AEDT) and create vehicle modeling methods beyond the current fixed wing and rotor-craft databases integrated in these models, where the primary focus was not on how noise results change according to trajectory definition [33–35].

In support of integrating future AAM configurations into the air traffic management system and understanding the

performance trade-offs that result from different vehicle-specific operational strategies, this work presents a physics-based methodology for assessing the performance and community noise of varied trajectories for distinct, defined AAM aircraft. A close examination of the definition of AAM control strategies for departure procedures for regions near airports for different vehicles is presented. Many AAM vehicle configurations are currently under development and being studied to determine their feasibility of performing AAM operations, including but not limited to electric, blown-flap short takeoff and landing vehicles (eSTOL), tilt-rotor electric vertical takeoff and landing vehicles (eVTOL), and lift plus cruise electric vertical takeoff and landing vehicles (eVTOL), as depicted in Fig. 1. Each AAM vehicle has unique performance capabilities stemming from differences in configuration such as different numbers of rotors, rotor designs, placement, load capacity, aerodynamic structure, and takeoff capability.

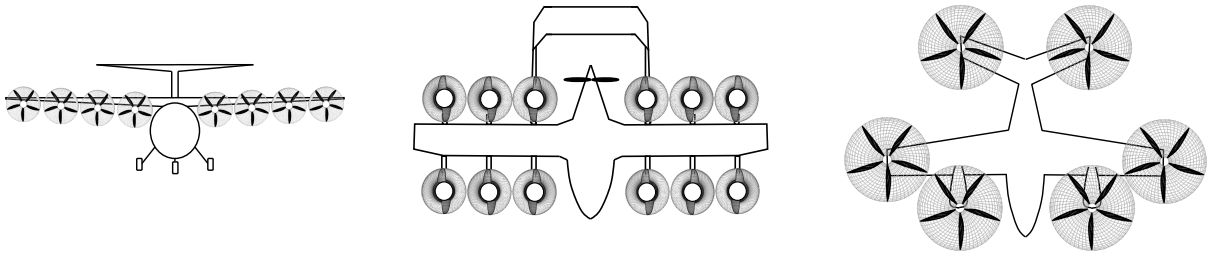

(a) Blown-Flap eSTOL (b) Lift plus Cruise eVTOL (c) Tilt-Rotor eVTOL

Fig. 1 Example AAM vehicle types referenced from [36].

The methodology presented in this paper is a tool for evaluating the capabilities of each of these distinct AAM aircraft architectures through the strategic design of flight trajectories based on the performance and dynamics of the unique vehicles presented in Fig. 1. Resulting trajectory performance metrics, including community noise impact, energy consumption, and flight duration are analyzed for strategically designed takeoff procedures to identify performance trade-offs resulting from varying procedures for each AAM aircraft architecture. The vehicles studied in this work are representative of diverse AAM aircraft architectures and each have vastly different performance capabilities and mission objectives, thus the intention of this work is not to compare the results across vehicles, but to analyze how the resulting performance metrics change for different departure procedures for each of the vehicles in Fig. 1.

The remainder of this paper is structured as follows: the analysis methodology is described in Section III with the framework for flight operation control strategy, aircraft performance, flight profile generation, source noise modeling, and trajectory integration provided in Sections III.A, III.B, III.C, III.D, and III.E respectively. The methodology is then applied to each of the three aircraft in Fig. 1 in Section IV, where the results for the Tilt-Rotor, Lift plus Cruise, and Blown-flap eSTOL vehicle are discussed in Sections IV.A, IV.B, and IV.C, respectively. Concluding comments and discussion are presented in Section V.

III. AAM Trajectory Design and Assessment Methodology

The AAM trajectory design and assessment framework is presented in Fig. 2. The design of a flight trajectory and evaluation of performance metrics including community noise, energy consumption, and flight duration, for a given AAM aircraft is initiated with a detailed aircraft architecture and control strategy for the flight operation.

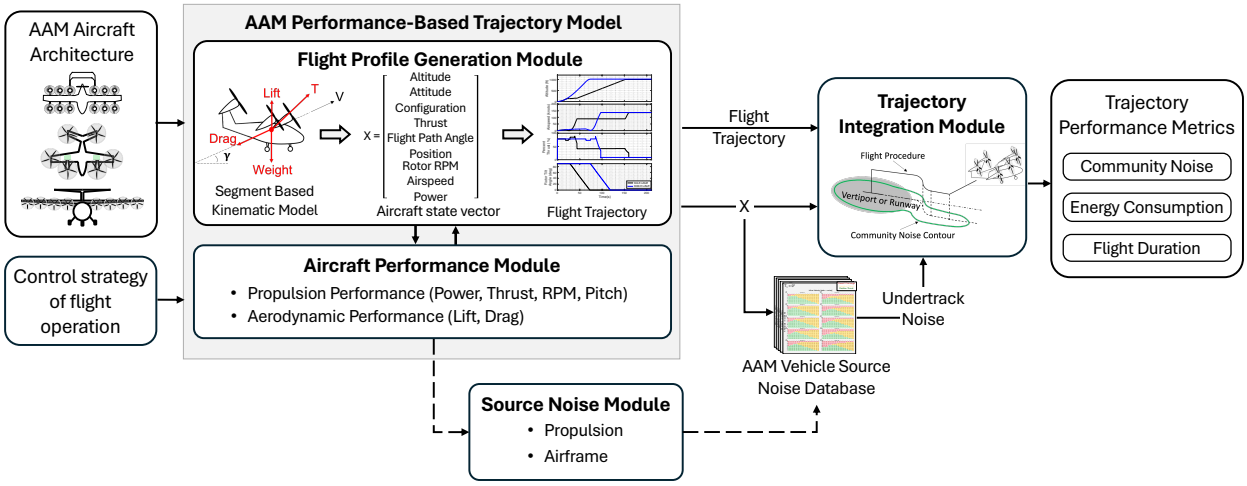

Fig. 2 Trajectory design and assessment framework for AAM vehicles.

The aircraft architecture encompasses the detailed geometry of the aircraft, known operating states, vehicle capacity, range, and unique configuration settings that the vehicle is intended to operate in. The vehicles that are evaluated in this paper are presented in Fig. 1 where this information is compiled according to publicly available data. These inputs are provided to the AAM Performance-Based Trajectory Model, which generates an aircraft state vector of the aircraft along a trajectory that meets the objectives of the control strategy, while accounting for the performance unique to the defined AAM aircraft. The state vector, denoted as X in Fig. 2, is generated within the Flight Profile Generation Module using a segment based force-balance-kinematic model, constrained by the vehicle performance characteristics from the Aircraft Performance Module and following flight instructions defined in the Control Strategy. Along with the Control Strategy, the aircraft state vector of the previous segment of the trajectory is used to compute the state vector of the next segment. In the Aircraft Performance Module, the aircraft characteristics such as wing shape, weight, rotor placement, and design conditions are utilized to determine the performance of the vehicle and propulsion system, leveraging the representative rotor designs and parametric drag build up of [36] and [37]. The details of these processes are included in Section III.B and III.C. Described in Section III.D, the Source Noise Module enables the evaluation of component noise levels for varying aircraft configurations and operational settings by modeling source noise of the aircraft's propulsion and airframe at each segment of the trajectory. The state vector, X, the flight trajectory, and the source noise database are inputs to the Trajectory Integration Module, where the resulting trajectory performance components: community noise, energy consumption, and flight duration, for the given operation and aircraft definition are calculated, as described in

Section III.E. A control strategy can only be executed for a given AAM aircraft with the performance capabilities to meet the desired flight operation. Further details and assumptions regarding the strategic design of control strategies for each AAM vehicle are described in Section III.A.

A. Control Strategy of Flight Operation

The high level inputs to the trajectory design and assessment framework in Fig. 2 are the AAM aircraft's architecture, as described in the previous section, and the control strategy of the flight operation intended to be flown by the vehicle. Flight objectives for each segment of a modeled trajectory are defined in the control strategy, such as those illustrated in Fig. 3, and include a combination of the aircraft configuration, desired flight path angle, and the thrust, power, or acceleration across the segment. The control strategy also includes the objective of the segment such as achieving a given altitude, velocity, flight path angle, or final configuration that indicates the end of a segment. Additionally, the methods for which the Aircraft Performance Module solves for rotor performance along the segment, as described in Section III.B, must be defined.

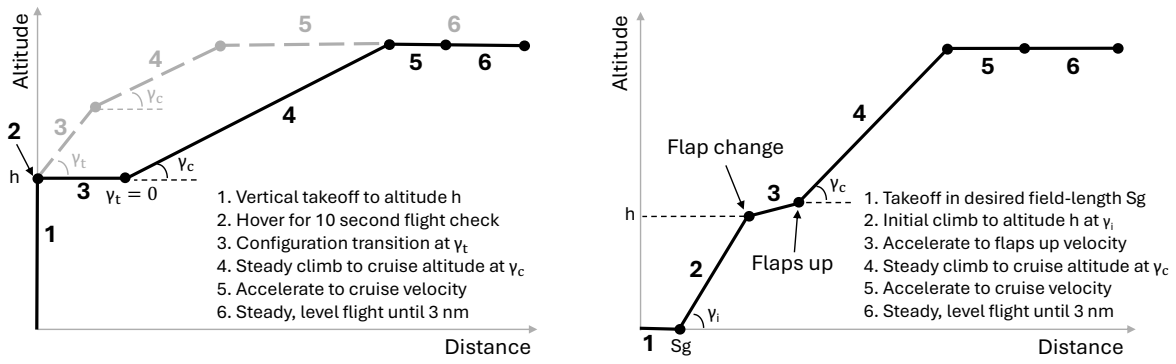

(a) eVTOL

(b) eSTOL

Fig. 3 Example control strategy for eVTOL and eSTOL AAM aircraft.

The performance of a given trajectory for a given AAM vehicle architecture is highly sensitive to the definition of the flight operation. Not all operations are feasible for all types of AAM aircraft, thus this framework assumes the user-defined control strategy is feasible for the aircraft being studied. The aircraft assessed in this study (see Fig. 1) are not all capable of performing the same flight profiles, for example, a STOL vehicle is not capable of vertical takeoff. Thus, the control strategy for vertical takeoff presented in Fig. 3a is not considered for the STOL vehicle, but rather the control strategy in Fig. 3b is used. Provided that the feasible range and performance objectives of a given AAM aircraft is assumed to be well understood, this framework is capable of assessing trajectory performance metrics of strategically designed trajectories. This provides a means for understanding the trade-offs between energy consumption, noise impact, and flight duration for a given AAM aircraft.

B. Aircraft Performance Module

The Aircraft Performance Module provides the aerodynamic and propulsion performance characteristics, according to the detailed description of the aircraft geometry, rotor geometry, vehicle configuration, and desired airspeed and throttle settings provided in the Aircraft Architecture and Flight Profile Generation Module. This framework leverages the AAM performance modeling methodology presented in [37] to determine the aerodynamic forces and detailed rotor performance, of which is necessary to model the dynamics and source noise of the aircraft. At each timestep over a flight segment, of which the vehicle orientation, configuration, desired airspeed and throttle settings are identified according to the control strategy, the lift, drag, thrust, rotor RPM and blade pitch are determined. The aircraft of this study, presented in Fig. 1, are assumed to be electric, and thus the weight of the aircraft is assumed constant. The lift of the vehicle is calculated according to the assumed aircraft characteristics such as wing area, airfoil dimensions and lift coefficients for each mode of flight, where eVTOL vehicles in a vertical lift configuration are assumed to have zero wing lift. The parabolic drag buildup from [37] that calculates parasitic and induced drag is referenced to predict the total vehicles drag, dependent on the assumed airspeed and aircraft configuration.

The propulsion performance considers the rotor RPM, thrust, power, pitch angle along with the rotor geometry, and inflow velocity using the blade element momentum rotor theory design tool, XROTOR [38], to determine rotor performance according to the vehicles state. Propellers describe a mechanical device that generates thrust force for the forward motion of a vehicle, are usually operated vertically, and are associated with fixed wing aircraft. This is distinct from rotors which directly produce both lift and thrust for a vehicle and can be operated both horizontally and vertically, as in the case of a tilting rotor. In this work, all propulsion devices are referred to as rotors. The assigned inflow velocity is assumed to be the component of the vehicle velocity vector that is perpendicular to the rotor disc, accounting for aircraft pitch, rotor tilt, and vehicle flight path angle as necessary. It is important to note, during transition phases, the impact of edgewise flight on blade loading is not captured in this modeling technique. Given a representative rotor designed uniquely for each vehicle architecture design condition [37] and the definition of the control strategy, unknown parameters are defined. For example, given the airspeed, required thrust, and desired RPM setting, the power and pitch angle of the rotor is defined by XROTOR. The design of representative rotors for each of the vehicles is referenced from [36] and [37].

The resulting propulsion and aerodynamic performance at a given instance is used in the Flight Profile Generation Module to build the flight dynamics and trajectory as described in Section III.C, and the rotor geometry and placement is necessary for the Source Noise Module to model the noise as described in Section III.D.

C. Flight Profile Generation Module

The Flight Profile Generation Module determines the flight dynamics using a time-stepped point mass model, constrained by the control strategy and AAM architecture, and influenced by the inertial effects of the aerodynamic loads

and propulsion performance from the Aircraft Performance Module, as depicted in Fig. 2. The necessary unknowns regarding the aircraft's performance within a given segment are calculated at each time step by the Aircraft Performance Module. The resulting flight parameters at each time step within a segment is stored in the aircraft state vector, X, and include altitude, attitude, vehicle configuration, thrust, flight path angle, position, rotor RPM, airspeed, and power. The state vector at the previous time step is used to compute the state of the aircraft for the next time step. This state vector accumulates into the flight trajectory, consisting of necessary details for determining the source noise of each segment as described in Section III.D, and for calculating the overall trajectory design outputs as described in Section III.E.

The point mass model, governed by the component level equations provided in eq. 1 and 2, is evaluated at time steps within each segment of the overall trajectory, where the flight objective of each segment is defined within the control strategy input introduced in Section III.A. Multirotor vehicles can be trimmed using variable pitch and RPM, or with control surfaces. In this work the vehicles are assumed to be trimmed with control surfaces.

$$T_x - Drag_x - Lift_x = ma_x \tag{1}$$

$$T_z - Drag_z + Lift_z - Weight = ma_z \tag{2}$$

The total thrust of the vehicle is the resultant vector of the components T_x and T_z of eq. 1 and 2. The thrust required for individual rotors (T) in eq. 3 is assumed to be uniform across operating rotors, and is therefore found by dividing the total thrust by the number of rotors considered to be operating (N_R), as defined by the control strategy.

$$T = \frac{\sqrt{T_x^2 + T_z^2}}{N_R} \tag{3}$$

D. Source Noise Module

When modeling the source noise of AAM vehicles within the framework presented in Fig. 2, it is assumed that the aircraft noise is composed of rotor and airframe source noise. These components of the source noise vary depending on the AAM vehicle type, configuration, rotor geometry, and operating conditions. The inputs to the source noise module include the vehicles speed, rotor RPMs, blade pitch, and aircraft configuration, see Fig. 4.

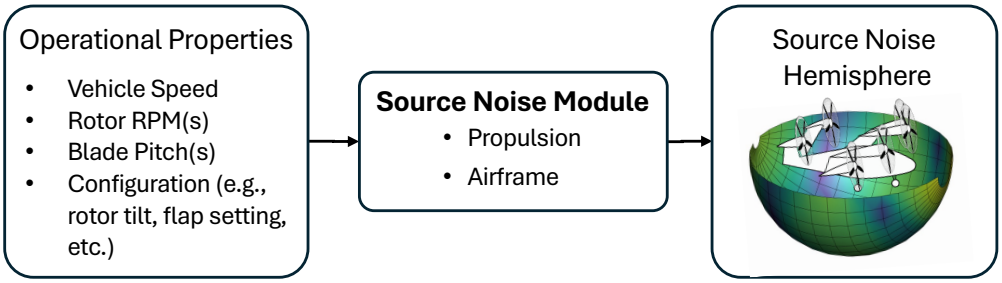

Fig. 4 Source Noise framework for AAM vehicles.

The output is a noise hemisphere for the given operating state. Used in the modeling of entire flight trajectories, as depicted in Fig. 2, is a source noise database of modeled noise according to feasible vehicle states. The AAM vehicles being studied, presented in Fig. 1, include open rotor, distributed propulsion, which is assumed to produce tonal and broadband noise components. Following the noise modeling procedure presented in [36], the NASA Aircraft NOise Prediction Program (ANOPP2) [39] is used, including features from the ANOPP2 Blade Element Acoustic Tool (ABEAT) [40] to model rotor tonal and broadband self noise, and the implementation of the Fink method [41] and Guo methods [42][43] in ANOPP for airframe trailing edge noise and high lift device and landing gear noise, respectively. Rotor loading is calculated within the ABEAT module using blade element momentum theory with blade geometry, such as feather angle, defined in the operating state vector. These results are used to model discrete loading and thickness noise using Farassat Formulation 1A methods [44], while broadband self noise from the rotor blade is modeled from semi-empirical methods [45], with the RPM and vehicle forward velocity defined in the state vector from the Flight Profile Generation Module, as described in Section III.C. Previous work has shown agreement of ABEAT modeled rotor noise to measured acoustic tests [46]. Following recommendations in [47], in order to obtain far-field noise values on the hemisphere surface, the radius of a source noise hemisphere was modeled such that the hemisphere surface was at least five rotor diameters away from the outermost rotor of the aircraft. The noise for each component is modeled as a source noise hemisphere as a function of frequency and directivity for each segment of the procedure, as defined in Fig. 3.

E. Trajectory Integration Module

The integration of the state vector and corresponding source noise along the segments that compose the trajectory for an AAM vehicle is done in the Trajectory Integration Module to determine the trajectory performance metrics: community noise, energy consumption, and flight duration. This provides a means for evaluating the performance of such metrics for a given AAM vehicle and control strategy, as well as compare them across operations.

Given modeled rotor and airframe noise sources along each segment, the community noise impact is generated by performing a propagation using ANOPP2 and based on atmospheric conditions and attenuation [48]. The final output of the community noise exposure is represented in metrics such as Maximum A-weighted sound pressure level ($L_{A,Max}$) and Sound Exposure Level (SEL). From the power setting determined using the blade element momentum rotor theory design tool, XROTOR, as described in the Aircraft performance Module (Section III.B) and the duration of each segment along the trajectory, the energy consumption is assumed by integrating the power over the duration of the trajectory. This provides a simplified method for understanding the energy consumption for the given operation, without a thorough understanding of the power train system. Lastly, the summation of the duration of each segment of the trajectory results in the flight duration for the operation, providing a means of understanding the duration of a given control strategy such as from takeoff to cruise altitude or velocity. In this paper, the flight duration is defined as the time from lift off in eVTOL operations and the start of takeoff roll in eSTOL operations, to when the aircraft is at cruise

altitude, and in cruise configuration for the given vehicle, at a groundtrack distance of 3 nm.

IV. Trajectory Design and Assessment Results of Sample Departure Procedures

A. Example Tilt-Rotor eVTOL Aircraft

Presented in this section is a comparison of various applications of a reference control strategy defined for the four passenger, 4000 lb Tilt-Rotor eVTOL vehicle with aircraft characteristics described in Section IV.A.1. A detailed description of the control strategy and cases studies are provided in Section IV.A.2, and the resulting trajectories and performance metrics are presented in Section IV.A.3.

1. Tilt-Rotor eVTOL Aircraft Characteristics

The Tilt-Rotor eVTOL aircraft has six, 5-bladed rotating rotors capable of providing thrust at any arbitrary rotor tilt angle, τ, between the vertical and horizontal direction, dependant on the requirement from the control strategy, as described in Section III.C. The x-direction and z-direction thrust per rotor, denoted by T_x and T_z, respectively are defined as the x and z components of the thrust vector per rotor, T, illustrated in Fig. 5. T_x and T_z are used to construct the flight profile according to eq. 1 and 2 as described in Section III.C.

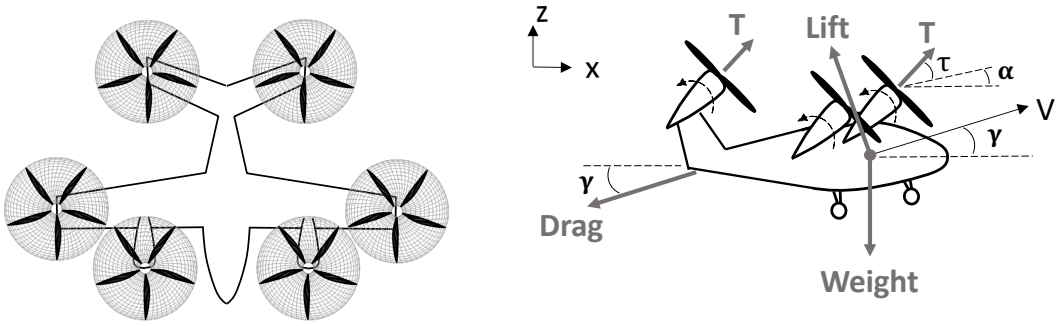

(a) Vehicle Configuration (b) Summary of Aerodynamic Forces

Fig. 5 Vehicle summary for 4000lb, 4 passenger Tilt-Rotor eVTOL [36].

The performance of the Tilt-Rotor eVTOL is highly dependant of the vehicle properties. Important vehicle properties assumed for this analysis are summarized in Table 1, including aircraft and propulsion characteristics. These properties are used within the Aircraft Performance Module as described in Section III.B to define the aerodynamic loads and rotor performance through the segments of the flight profile that are defined according to the control strategy outlined in the next section (Section IV.A.2). The maximum power, RPM, and thrust of the propulsion system are assumed according to the rotor designed for this vehicle from [37].

Table 1 Tilt-Rotor eVTOL vehicle properties, referenced from [36, 49], used for example trajectory design analysis.

Aircraft Characteristics	Weight (lbs)	4000
	Number of Passengers	4
	Span (ft)	35
	Cruise Speed (kts)	152
Propulsion Characteristics	Maximum Power per Rotor (kW)	125
	Maximum RPM of Rotor	800
	Maximum Thrust per Rotor (lb)	867
Rotor Geometry	Rotor Diameter (ft)	9.5
	Number of Rotors	6
	Number of Blades per Rotor	5
	Hub Percent of Rotor Diameter (%)	10
	Rotor image	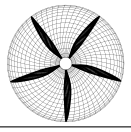

2. Control Strategy for Sample Departure Procedures of Tilt-Rotor eVTOL

The control strategy, as depicted in the framework in Fig. 2, is a segmented flight objective for the desired procedure. In this study, the eVTOL control strategy introduced in Fig. 3a of Section III.A is adapted for the Tilt-Rotor vehicle as summarized in Fig. 6 for four departure procedures.

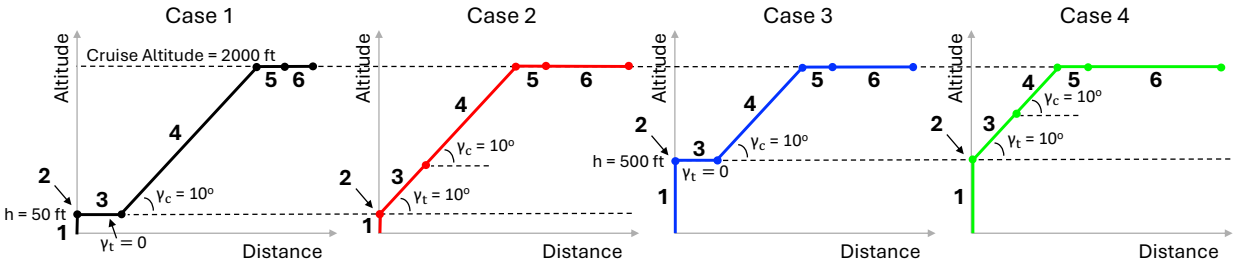

Fig. 6 Comparison of 4000 lb, 4 passenger Tilt-Rotor eVTOL flight profiles.

The four variations of departure trajectories include changes in the acceleration altitude (denoted as h) that the vertical takeoff is constrained by, and the flight path angle (γ_t) of the transition (segment 3). As summarized in Table 2,

trajectories either vertically climb to 50 ft or 500 ft, and the transition occurs either level, or while climbing at 10°.

Table 2 Tilt-Rotor eVTOL trajectories analyzed in case study.

Case Number	Description
Case 1	50 ft hover, level transition
Case 2	50 ft hover, 10° climbing transition
Case 3	500 ft hover, level transition
Case 4	500 ft hover, 10° climbing transition

The control strategy is divided into six segments, each of which constrain the vehicle to a desired condition and is described below.

Segment 1: The vertical takeoff segment constrains the rotors of the Tilt-Rotor vehicle to 90° from the horizontal. The total thrust of the vehicle is set to a constant 102% of the vehicles weight, thus resulting in vertical flight. As described in Section III.B, the aircraft performance module determines the power and rotor pitch necessary for this operation, and the dynamics of the vehicle is resolved to determine the aircraft's velocity and acceleration. In vertical flight the lift of the wing is assumed to be zero.

Segment 2: The hover segment begins when the acceleration altitude, h, is reached. The thrust then drops to 100% of the vehicles weight, and the vehicle remains in a hovering state for a notional 10-second flight check.

Segment 3: During the transition segment, the rotor's tilt follows a velocity-based schedule from the vertical, 90° configuration, to the horizontal, 0° configuration. The rotor's tilt is measured from the angle of attack, α, of the aircraft (see Fig.5b). This velocity-based tilt schedule was derived by resolving the vehicle dynamics at various degrees of rotor tilt. As the rotor tilts towards horizontal, the direction of the thrust vector changes, resulting in acceleration in the horizontal direction and a loss of vertical thrust. As the vehicle accelerates, an increase in horizontal velocity increases the lift from the wing. In order to maintain altitude or the desired flight path angle, γ_t, the rotor tilt angle, τ, is scheduled at a velocity such that the gained lift is equal to the loss in vertical thrust from the rotors. During the transition segment it is assumed the aircraft has an angle of attack of 12° according to [50]. Upon completion of transition, the vehicle has accelerated to a velocity that results in the vertical forces equal to the weight.

Segment 4: The vehicle climbs at a desired flight path angle, γ_c, to cruise altitude at constant velocity, holding constant propulsion conditions. The velocity of this segment is assumed to be constant with the final velocity from segment 3. This tilt-rotor vehicle is capable of climbing at a γ_c of 10° at a 12° angle of attack. In this study, cruise altitude is assumed to be 2000 ft.

Segment 5: Upon reaching cruise altitude, the aircraft begins to accelerate and level out to cruise conditions,

assuming the cruise velocity to be the best cruise speed of 112 kts, as determined in [51] with an angle of attack of 6°.

Segment 6: The vehicle remains in cruise configuration for the remainder of the trajectory, until reaching a groundtrack distance of 3 nm.

The resulting trajectories and corresponding performance are presented in Section IV.A.3 to demonstrate how the vehicle performance changes according to the flight trajectory.

3. Trajectory Design Results of Sample Departure Control Strategies

The methodology presented in Section III is applied to the Tilt-Rotor eVTOL according to the control strategy presented above in Section IV.A.2. The resulting trajectories are compared in Fig. 7 as a function of time, where interfaces between segments that displayed nonlinearities were smoothed. This figure illustrates the changes in aircraft state, denoted as X in the framework in Fig. 2, and the aerodynamic and propulsion performance. For visual inspection, the altitude is plotted at the top of both columns. Key differences between the cases include the time at which the aircraft reaches cruise altitude, cruise velocity, and where changes in aircraft performance occur. Cases 1 and 2 have a lower constraint on the vertical climb, and reach cruise altitude earlier, where Case 2, the climbing transition, reaches cruise altitude first. Likewise, the cases reach the end of the departure trajectory in the same order, with little differences between cases with the same vertical takeoff altitude. However, Cases 1 and 2 remain at a lower altitude for longer in the beginning of the trajectory, thus performing the transition segment of the control strategy at a lower altitude, and earlier in the trajectory. Increasing the flight path angle during transition (γ_t) results in a subtle difference in acceleration, but allows the aircraft to reach a higher altitude, as evident for Cases 2 and 4.

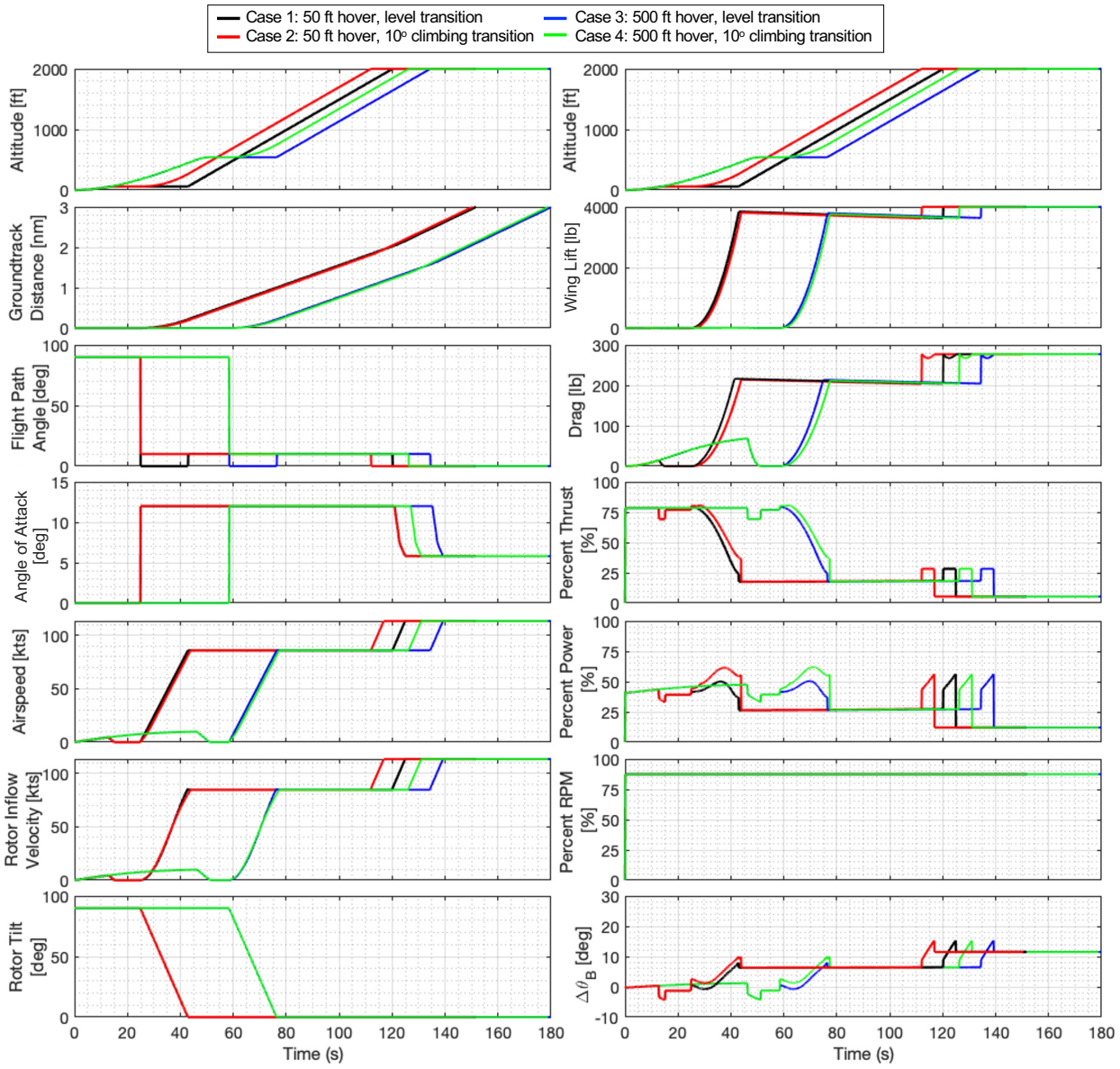

Fig. 7 Comparison of 4000 lb, 4 passenger Tilt-Rotor eVTOL flight profiles.

As each of the cases presented in Fig. 7 follow the same control strategy, they follow similar trends across the flight profile, but performed at different times. This provides a means for identifying the impact that the vertical lift altitude (h) and the transition climb angle have on the aircraft's energy and community noise impact. The trajectory performance is summarized in Fig. 8, including a plot for the cumulative total energy over time, and the undertrack noise plotted as overall A-weighted sound pressure level ($L_{A,Max}$) and sound exposure level (SEL) modeled according to the methodology presented in Section III.D. As presented in Fig. 8, there is a trade-off between undertrack noise, energy, and time depending on the altitude reached on vertical takeoff (h). The higher vertical takeoff, Cases 3 and 4, result in more energy and time but produce lower undertrack noise levels early in the trajectory as well as an overall quieter

observed noise level during transition. Thus, gaining altitude early in the trajectory is advantageous for community noise for this vehicle. The resulting undertrack noise presents comparable noise levels at a similar condition to the reported noise level of 45 dBA at 1640 ft altitude and 100 kts airspeed published by vehicle manufacturers of similar tilt-rotor configurations [52], with contour areas comparable to the flight test results presented in [53].

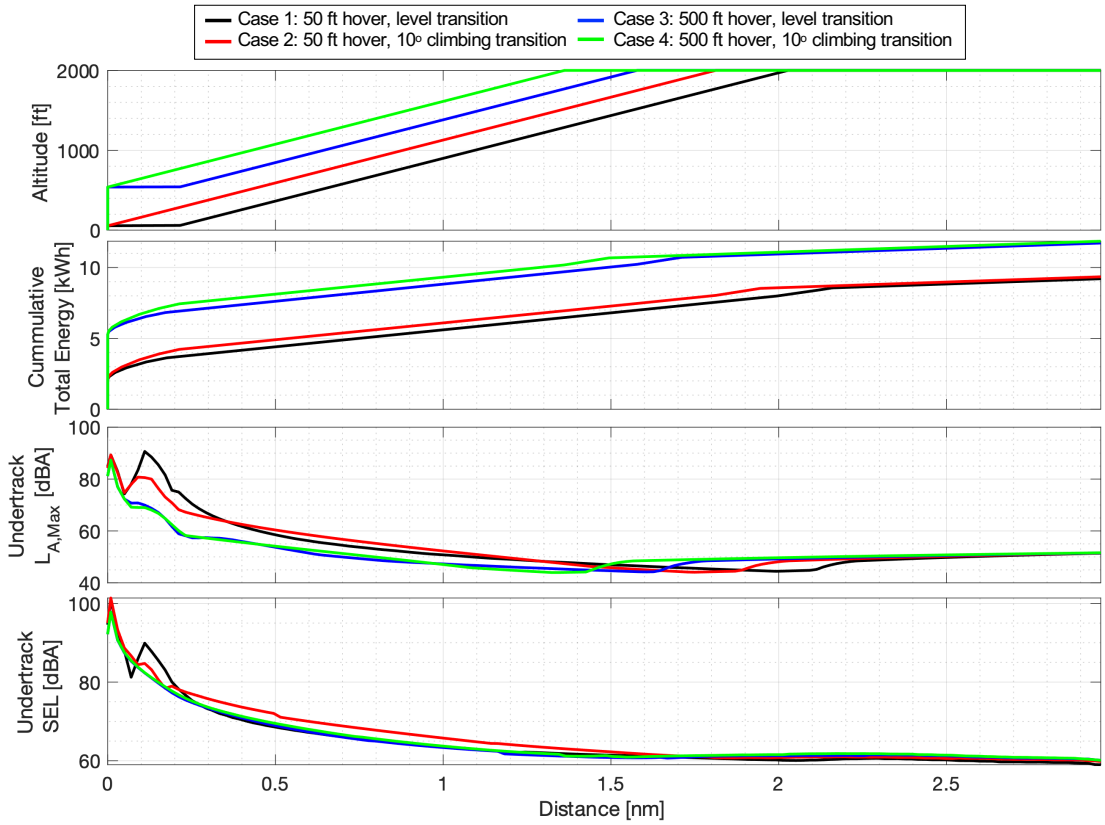

Fig. 8 Trajectory performance results of 4000 lb, 4 passenger Tilt-Rotor eVTOL case studies.

Noise contours, shown in Fig. 9, are used to compared the community noise impacts of each takeoff trajectory. All four tilt-rotor contours at both medium and high $L_{A,Max}$ levels are teardrop-shaped with the widest point of the contour surrounding the takeoff origin and an elongated tail following the direction of flight.

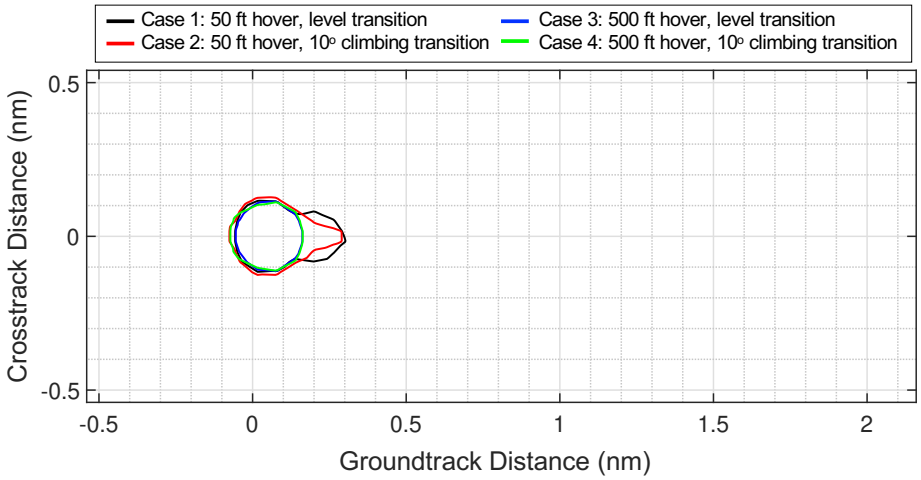

Fig. 9 65 dBA $L_{A,Max}$ single event noise contours for 4000 lb, 4 passenger Tilt-Rotor eVTOL trajectories.

Compared to Case 1, the steeper transition angle of Case 2 results in a more tapered noise contour as the vehicle departs. At the takeoff origin, the contour for Case 2 has a slightly larger radius compared to Case 1, however, this is a less pronounced change in area compared to the taper. In contrast, Cases 3 and 4 are quite similar in shape and area, being concentric circles of similar radii. The effect of transition angle seem to have little effect in changing contour area and shape for Cases 3 and 4. The contour area from Case 1 to 2 decreased by 0.04 nm^2 while Cases 3 to 4 showed no area change.

A summary of the overall trajectory performance including the 65 dB $L_{A,Max}$ contour area, the total energy, and the time the aircraft takes to reach the end of the departure procedure is presented in Table 3. The contour areas for Cases 3 and 4 have the same and smallest size, thus the differences in these trajectories do not impact the 65 dB noise level. However, the higher vertical takeoff altitude does take longer and require more energy. Case 1 required the least amount of energy, but Case 2 is slightly faster with minimal increase in energy due to the climbing transition.

Table 3 Tilt-Rotor eVTOL performance results for departure trajectories.

Case Number	Vertical Takeoff Altitude (ft)	Transition Climb Angle (deg)	65 dBA $L_{A,Max}$ Noise Contour Area (nm^2)	Total Energy (kWh)	Flight Duration (s)
Case 1	50	0°	0.059	9.2	152
Case 2	50	10°	0.058	9.4	150
Case 3	500	0°	0.038	11.8	180
Case 4	500	10°	0.041	11.9	179

B. Example Lift plus Cruise eVTOL Aircraft

Presented in this section is a comparison of various applications of a reference control strategy defined for the 2 passenger, 2800 lb Lift plus Cruise vehicle with aircraft characteristics described in Section IV.A.1. A detailed description of the control strategy and cases studies are provided in Section IV.A.2 and the resulting trajectories and performance metrics are presented in Section IV.A.3.

1. Lift plus Cruise eVTOL Aircraft Characteristics

The Lift plus Cruise eVTOL is capable of vertical and forward flight through two independent propulsive systems, as presented in Fig. 10a. The horizontal rotor is the primary source for horizontal thrust denoted as T_c, while the lifting rotors are the primary source of vertical thrust in vertical flight, where their thrust per rotor is denoted as T_L. The thrust of each rotor is assumed to be perpendicular to the rotors disc, where the disc position changes according to the vehicles Angle of Attack (α). Thus, the total thrust in the x and z directions are a combination of the directional components of the thrust produced from each rotor. Figure 10b displays that the inertial properties utilize the assumption that the thrust vectors are fixed with respect to the vehicles airframe throughout the flight procedure.

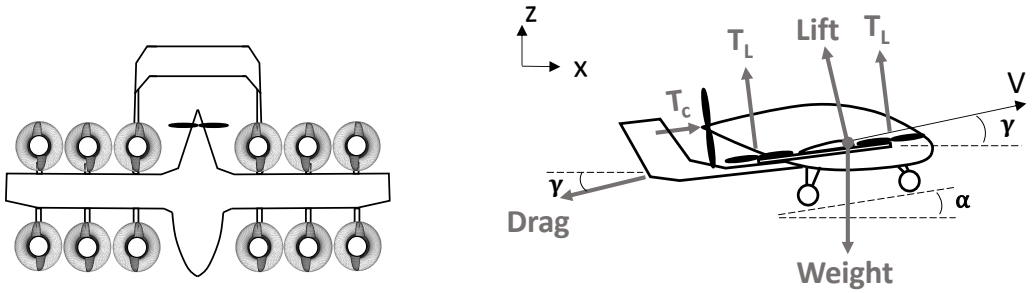

(a) Vehicle Configuration

(b) Summary of Aerodynamic Forces

Fig. 10 Vehicle summary for a 2800 lb, 2 passenger Lift plus Cruise eVTOL [36].

The key vehicle properties used to model this Lift plus Cruise aircraft are summarized in Table 4, where the aircraft characteristics, rotor tip mach, hub diameter, and blade count are referenced from [54]. The rotor design and propulsion characteristics are referenced from [37], which sized the lifting and cruising rotors according to design conditions outlined in [54].

Table 4 Lift plus Cruise eVTOL vehicle properties [37, 54].

Aircraft Characteristics	Weight (lbs)		2800
	Number of Passengers		2
	Span (ft)		36
	Cruise Speed (kts)		96
Propulsion Characteristics	Maximum Power per Rotor (kW)	Lift Rotors	27
		Cruise Rotor	98
	Maximum RPM of Rotor	Lift Rotors	2900
		Cruise Rotor	1700
	Maximum Thrust (lb)	Lift Rotors	1350
		Cruise Rotor	1257
Known Rotor Geometry	Rotor Diameter (ft)	Lift Rotors	4.3
		Cruise Rotor	6.6
	Number of Rotors	Lift Rotors	12
		Cruise Rotors	1
	Number of Blades per Rotor	Lift Rotors	2
		Cruise Rotors	3
	Hub Percent of Rotor Diameter (%)	Lift Rotor	30
		Cruise Rotor	20
	Rotor image	Lift Rotors	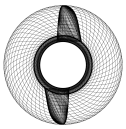
		Cruise Rotor	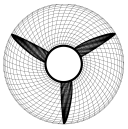

2. Control Strategy for Sample Departure Procedures of Lift plus Cruise eVTOL

The Control Strategy of the Lift plus Cruise vehicle follows that of the eVTOL, presented in Fig. 3a, but adapted to the specific characteristics of the Lift plus Cruise vehicle outline in the previous section (Section IV.B.1). The control strategy applied to the four cases studied for the Lift plus Cruise vehicle are detailed in Fig. 11, below.

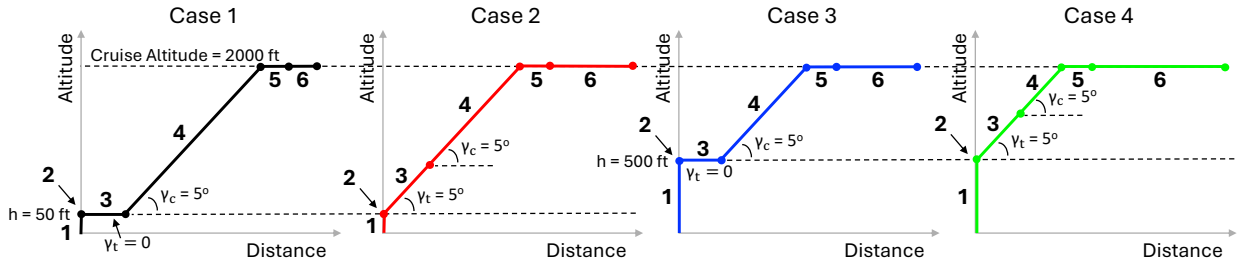

Fig. 11 eVTOL Control Strategy applied to four departure procedures for the Lift plus Cruise vehicle.

The four variations of departure trajectories include changes in the altitude (denoted as h) that the vertical takeoff is constrained by, and the flight path angle, γ_t, of the transition (segment 3). As summarized in Table 5, trajectories either vertically climb to 50ft or 500ft, and the transition occurs either level, or while climbing at 5°.

Table 5 Lift plus Cruise eVTOL trajectories analyzed in case study.

Case Number	Description
Case 1	50 ft hover, level transition
Case 2	50 ft hover, 5° climbing transition
Case 3	500 ft hover, level transition
Case 4	500 ft hover, 5° climbing transition

The control strategy constrains the vehicle along segments of the trajectory to a desired condition as follows.

Segment 1: A vertical takeoff, constraining the vehicle's propulsion to only the lifting rotors, setting the total thrust of the 12 lifting rotors to a constant 102% of the vehicles weight, thus resulting in vertical flight. The propulsion performance is resolved according to the procedure detained in Section III.B for the power and rotor pitch. The dynamics of the vehicle is resolved by adapting eq.1 and 2 in Section III.C to the Lift plus Cruise dynamics of Fig. 10b to determine the aircraft's velocity and acceleration. In vertical flight, the lift of the wing is assumed to be zero.

Segment 2: When the desired altitude, h, is reached, the total thrust of the lifting rotors drops to 100% of the weight, and the vehicle remains in a hover state for a notional 10-second flight check.

Segment 3: From hover, the vehicle enters a transition phase where the cruise rotor is turned on to max RPM and the vehicle begins to accelerate in the horizontal direction, increasing the aerodynamic lift and decreasing the thrust required from the lifting rotors to maintain the desired flight path angle. This segment ends at a velocity where the total vertical force, including aerodynamic lift and the vertical force of the cruise rotor if at a positive angle of attack, is enough for the lifting rotors to be turned off. In non-vertical flight, the inflow velocity of the lifting rotors is assumed to be zero.

Segment 4: After transitioning to cruise configuration, the vehicle begins a constant velocity climb at 5° with the cruise rotor at max RPM and an angle of attack of 12° until a cruise altitude of 2000 ft.

Segment 5: When cruise altitude is reached, the vehicle accelerates to cruise velocity and levels off to cruise condition. The cruise velocity for the Lift plus Cruise vehicle is assumed to be 90% of the maximum cruise speed from [54].

Segment 6: The vehicle remains in cruise condition for the remainder of the trajectory, until a groundtrack distance of 3 nm is reached.

The cases summarized in Table 5 are presented in the following section, where the resulting differences in flight profiles and trajectory performance are compared.

3. Trajectory Design Results of Sample Departure Operation Definitions

The control strategy summarized above is applied to the Lift plus Cruise eVTOL and the resulting trajectories for the cases in Table 5 are compared in Fig. 12, where interfaces between segments that displayed nonlinearities were smoothed. Plotted over time, the flight profiles in Fig. 12 illustrate the changes in aircraft state, denoted as X in the methodology in Fig. 2, and the aerodynamic and propulsion performance. For visual inspection, the altitude is plotted at the top of both columns. It can be seen from the propulsion data that the transition segment starts for Cases 1 and 2 when the cruise rotor turns on at 25 seconds, and ends when the lift rotor turns off at approximately 75 seconds for Case 1 and 110 seconds for Case 2. Likewise, for the higher altitude case, the transition duration is the same lengths for the respective transition climb angles. This illustrates the impact on the acceleration rate that the transition flight path angle, γ_t, has on the procedure. The acceleration rates of the transition segments are significantly slower for cases that transition while climbing, indicating that a transition while climbing requires the lifting rotors to be on for a longer duration of the flight, but the aircraft is gaining altitude at the same time.

Similar to the results from the Tilt-Rotor, other notable differences in the resulting procedures include the time at which the aircraft reaches cruise altitude, cruise velocity, and the time at which changes in aircraft performance occur. Like the Tilt-Rotor, a lower altitude constraint on the vertical climb results in reaching cruise altitude slightly earlier. However, for the Lift plus Cruise vehicle, the level transition case reaches cruise altitude earliest, primarily due to the more notable difference in acceleration rates. When comparing the transitions segments, it can be seen in Fig. 12 that Case 2 and Case 3 turn off their lifting rotors at nearly the same time. However, Case 2 reaches cruise altitude and the end of the departure trajectory before Case 3, suggesting that a climbing transition is more advantageous in gaining distance and altitude on departure as opposed to a vertical climb. Evaluating the groundtrack distance at which the aircraft reach cruise altitude, it is evident that the cases with a lower vertical takeoff altitude, h, (Cases 1 and 2) reach cruise altitude further from the takeoff, in groundtrack distance, than the cases with a higher vertical takeoff altitude. Thus, the higher vertical climb performs the entire departure operation at a higher altitude than the other cases.

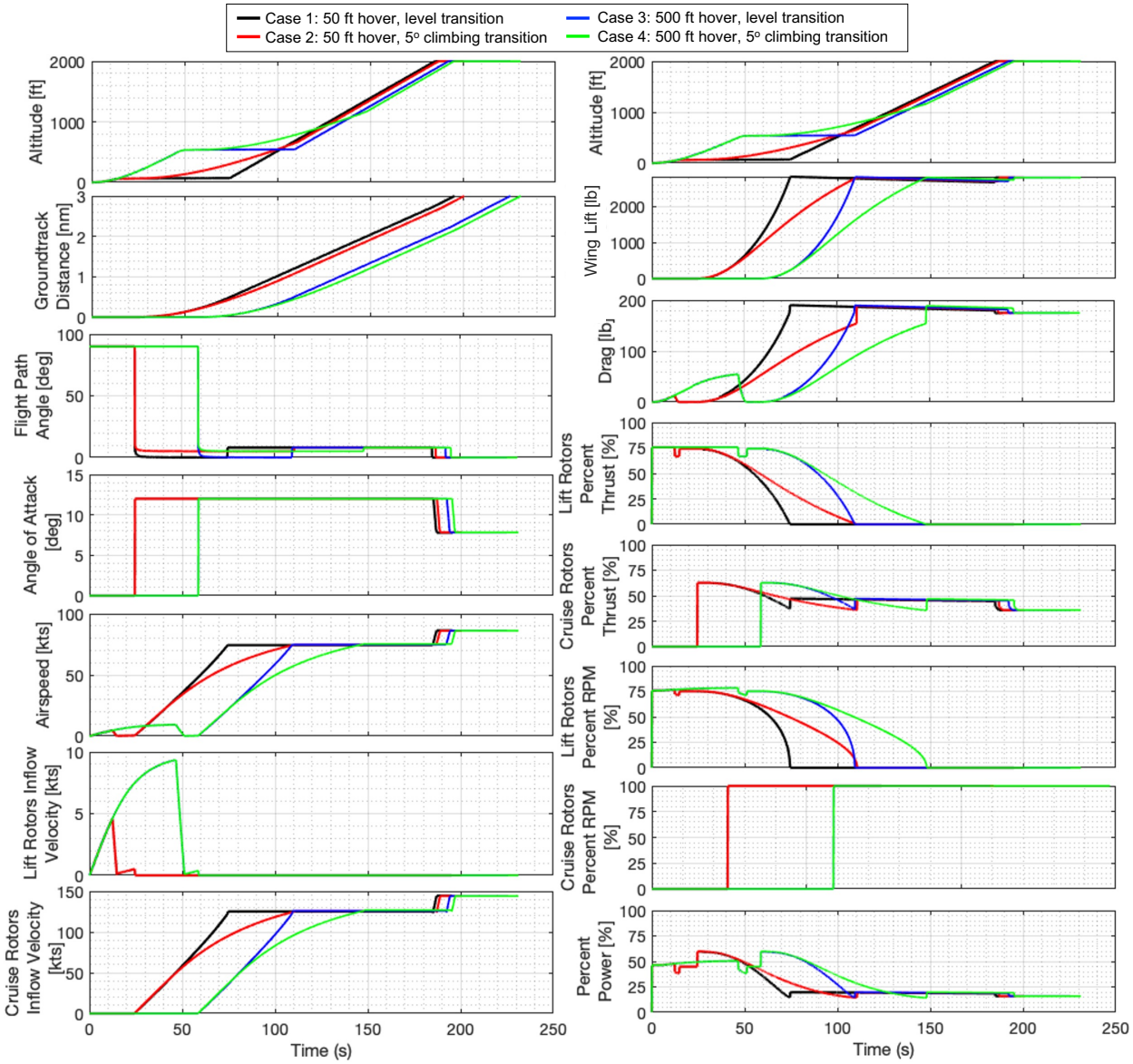

Fig. 12 Comparison of 2800 lb, 2 passenger Lift plus Cruise eVTOL flight profiles.

It can be seen in the flight profiles summarized in Fig. 12 that the different cases follow the same control strategy, but the differences in vertical takeoff altitude and transition climb angle result in different magnitudes of changes and segments occur at different times. The various differences in the flight profiles thus result in different energy consumption, flight duration, and community noise impact. These trajectory performance metrics are summarized in Fig. 13, including a plot for the cumulative total energy over time, and the undertrack noise plotted both as $L_{A,Max}$ and SEL. These performance metrics were modeled according to the methodology presented in Section III.E. As presented in Fig. 13, there is a visible trade-off between undertrack noise, energy, and time depending on the altitude reached on vertical takeoff (h). Case 1 consumes overall the least amount of energy and reaches the end of the departure procedure earliest,

however has the highest undertrack noise levels during the vehicle transition, which remains at the lowest altitude for longest. Additionally, there is a notable spike in undertrack noise during the transition segment of the flight procedure for Cases 1 and 3, where the aircraft does not climb during transition. Thus, with little impact on energy consumption, a climbing transition segment can potentially provide community noise benefits for the Lift plus Cruise vehicle.

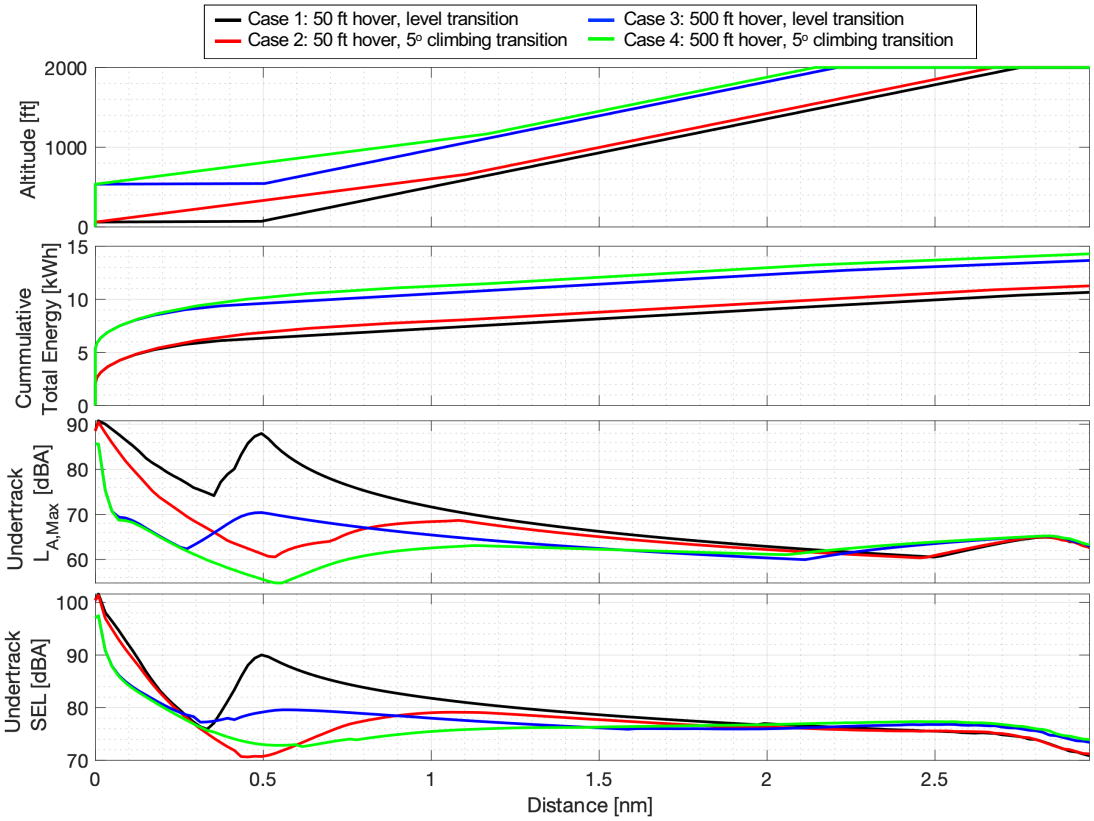

Fig. 13 Trajectory performance results of 2800 lb, 2 passenger Lift plus Cruise eVTOL case studies.

The noise contours for the Lift plus Cruise cases are presented in Fig. 14. Each contour has two distinct regions, a rounded contour surrounding the takeoff origin where the lift rotors are operational, and an elongated elliptical shape where the cruise rotor starts and the vehicle moves away from the origin.

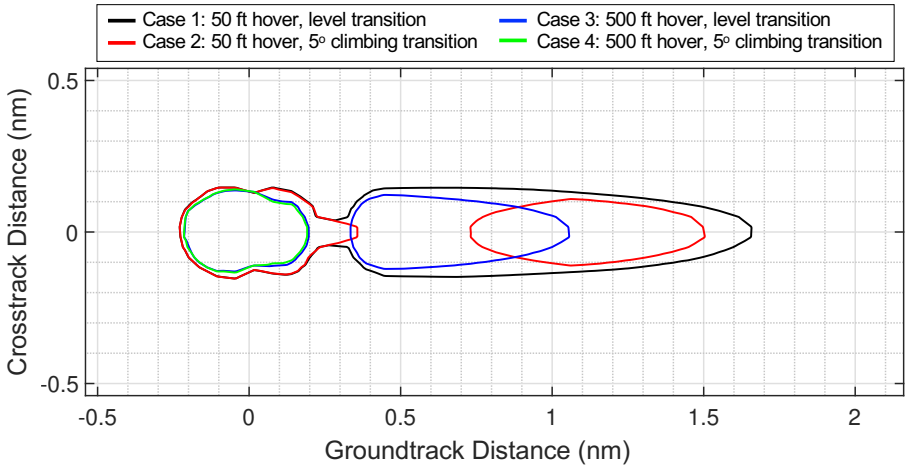

Fig. 14 65 dBA $L_{A,Max}$ single event noise contours for 2800 lb, 2 passenger Lift plus Cruise eVTOL trajectories.

At the point of lift and cruise rotor transition, Case 1 shows a sharp reduction in contour width while Case 2 becomes two distinct contours about the takeoff origin and transition ground-track areas. Generally, there is a decrease in contour area associated with an increase in transition flight path angle, γ_t. From Cases 1 to 2, there is an area reduction of 0.20 nm^2, while operating from Case 3 to 4 yields a reduction of 0.12 nm^2. A summary of the overall trajectory results are presented in Table 6. Case 4 presents the smallest noise contour area, but requires the most energy and has the longest flight duration. Case 1 requires the least amount of energy and is the fastest procedure, but has the largest noise contour area.

Table 6 Lift plus Cruise eVTOL performance results for departure trajectories.

Case Number	Vertical Takeoff Altitude (ft)	Transition Climb Angle (deg)	65 dBA $L_{A,Max}$ Noise Contour Area (nm^2)	Total Energy (kWh)	Flight Duration (s)
Case 1	50	0°	0.44	10.7	196
Case 2	50	5°	0.24	11.3	201
Case 3	500	0°	0.21	13.7	226
Case 4	500	5°	0.09	14.3	231

C. Example Blown-Flap eSTOL AAM Aircraft

A comparison of applications of a 9 passenger, 6000 lb Blown-Flap eSTOL reference control strategy is presented. Notable aircraft characteristics that impact the definition of the control strategy for the Blown-Flap eSTOL are detailed in Section IV.C.1. The control strategy for the cases studies of this vehicle are provided in Section IV.C.2, and the resulting trajectories and performance metrics are discussed in Section IV.C.3.

1. Blown-Flap eSTOL Aircraft Characteristics

The Blown-Flap eSTOL vehicle illustrated in Fig. 15a, functions similar to a traditional fixed-wing aircraft. However, the unique short takeoff and landing capabilities of this vehicle are achieved through distributed propulsion and blown flap technology as outlined in [55] and summarized in Fig. 16. The rotors that line the leading edge of the wing produce a jet, V_j, of increased velocity compared to the airspeed of the vehicles. The increased jet velocity of the flow over the flaps provides higher C_L values at lower airspeeds. Thus, a blown-flap results in lower required takeoff velocities, allowing the vehicle to takeoff in shorter distances. The total thrust of the rotors is assumed to be in the direction of flight, with flight path angle denoted as γ shown in Fig. 15b.

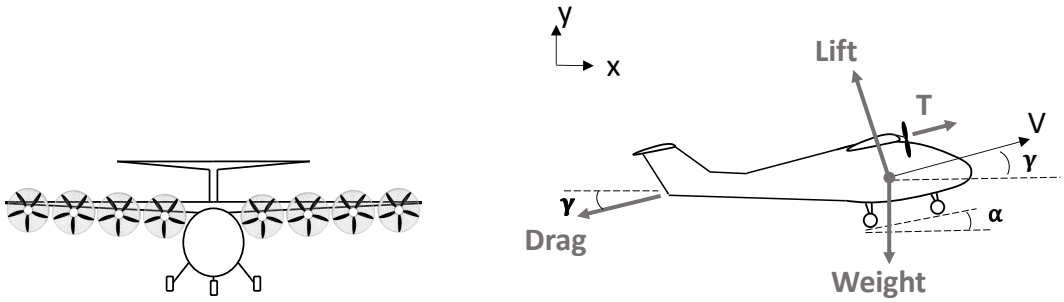

(a) Vehicle Configuration (b) Summary of Aerodynamic Forces

Fig. 15 Vehicle Summary for 6000 lb, 9 passenger Blown-Flap eSTOL [36].

Due to the increased velocity of the rotor wake, the blown-flap induces an additional source of drag, which is determined via the momentum theory of jet contraction, following the analysis in [56] and is captured within the drag buildup [37] included in the Aircraft Performance Module outlined in Section III.B.

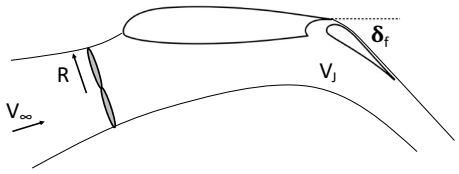

Fig. 16 Rotor wake interaction with the flap in Blown-Flap eSTOL aircraft [36].

The lift coefficients of the blown-flap are determined according to the vehicles airspeed, angle of attack, and jet velocity (V_j) at a given state by referencing blown-flap wind tunnel data in [55]. The inertial properties are calculated by determining the aerodynamic forces in Fig. 15b according to the methods described in Section III.B and adapting the equations of motion highlighted in eq.1 and 2 in Section III.C to the Blown-Flap eSTOL. Significant vehicle properties assumed for the Blown-Flap eSTOL to model the flight performance including aircraft and propulsion characteristics, as well as known rotor geometry are described in Table 7, where the rotor design is referenced from [37]. This vehicle is assumed to achieve a 150 ft takeoff field length at maximum power, as indicated in [56], with a takeoff velocity of 38

kts. The propulsion characteristics are assumed according to the rotor design published in [37] and the cruise speed is assumed according to the data presented in [56].

Table 7 Blown-Flap eSTOL vehicle properties, referenced from [56] and [57].

Aircraft Characteristics	Weight (lbs)	6000
	Number of Passengers	9
	Span (ft)	43.7
	Cruise Speed (kts)	150
Propulsion Characteristics	Maximum Power per Rotor (kW)	90
	Maximum RPM of Rotor	4000
	Maximum Thrust per Rotor (lb)	352
Known Rotor Geometry	Rotor Diameter (ft)	2.7
	Number of Rotors	8
	Number of Blades per Rotor	5
	Hub Percent of Rotor Diameter (%)	25
	Rotor image	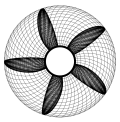

2. Control Strategy for Sample Departure Procedures of Blown-Flap eSTOL

The control strategy constraining for the Blown-Flap eSTOL vehicle defines segments of the flight trajectory similar to that of a conventional aircraft. The control strategy outlined Fig. 3b of Section III.A is applied to this Blown-Flap eSTOL for four variations of departure procedures as depicted in Figure 17.

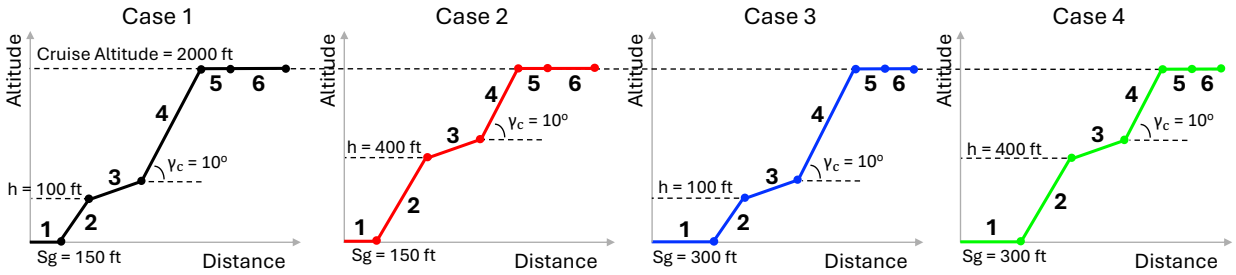

Fig. 17 eSTOL Control Strategy applied to four departure procedures for the Blown-Flap eSTOL vehicle.

The four variations of departure trajectories include changes in the takeoff field length and acceleration altitude (h). As summarized in Table 8, trajectories either takeoff in 150 ft at maximum RPM, or in 300 feet at 80% maximum RPM.

For this aircraft, the 150 ft takeoff is assumed to use a flap detent, δ_f, of 20° and the 300 ft takeoff requires a flap detent of 40° in order to produce enough lift at the same takeoff velocity of 38 kts with a lower jet velocity V_j from the lower takeoff RPM setting.

Table 8 Blown-Flap eSTOL trajectories analyzed in case study.

Case Number	Description
Case 1	150 ft takeoff field-length, initial climb to 100 ft at 100% RPM
Case 2	150 ft takeoff field-length, initial climb to 400 ft at 100% RPM
Case 3	300 ft takeoff field-length, initial climb to 100 ft at 80% RPM
Case 4	300 ft takeoff field-length, initial climb to 400 ft at 80% RPM

The control strategy constrains the vehicle along segments of the flight trajectory to a desired condition, defined as follows.

Segment 1: The takeoff segment is defined according to the desired takeoff field length, determining the power or RPM required at takeoff. This vehicle is capable of a 150ft takeoff field length at max power. By lowering the power on takeoff, the takeoff field length will increase and the vehicle will have less power on the initial climb, as the initial climb assumes the same power setting from the takeoff segment.

Segment 2: The initial climb assumes constant conditions to that of segment 1, and the flight path angle of the initial climb, γ_i, is determined. At maximum power, the vehicle climbs at a γ_i of 10°. The vehicle climbs in the defined takeoff condition until the desired acceleration altitude, h.

Segment 3: When the vehicle reaches the acceleration altitude, h, the vehicle will lower the climb rate to accelerate to the flaps up velocity of 70 kts. If a higher flap detent was used during takeoff, the flaps are retracted to 20°. For the cases studied, this acceleration segment starts at either an altitude of 100 or 400 feet.

Segment 4: Upon retracting the flaps, the aircraft climbs at constant velocity at a γ_c of 10° until cruise altitude.

Segment 5: At cruise altitude, assumed to be 2000 ft, the aircraft levels out and accelerates to cruise conditions.

Segment 6: Cruise conditions are held until the aircraft reaches 3 nm groundtrack distance.

The resulting trajectories are analyzed in Section IV.C.3 to demonstrate how the vehicle's performance changes according to the departure procedure.

3. Trajectory Design Results of Sample Departure Control Strategies

The methodology presented in Section III is applied to the Blown-Flap eSTOL according to the control strategy presented in Section IV.A.2 for the four variations summarized in Table 8. The resulting trajectories are compared in Fig. 18 as a function of time, where interfaces between segments that displayed nonlinearities were smoothed. For

visual inspection, the altitude is plotted at the top of both columns.

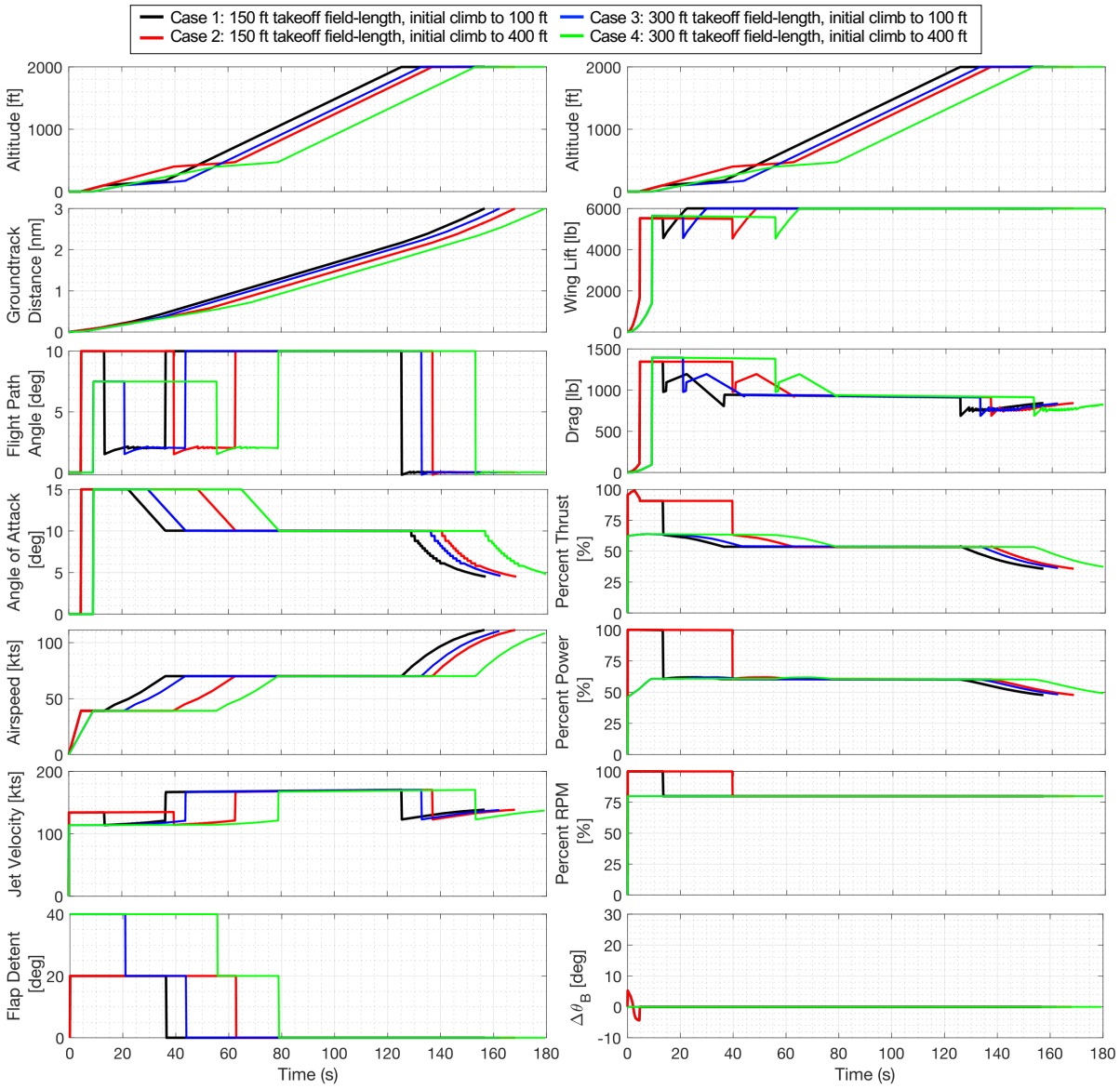

Fig. 18 Comparison of 6000 lb, 9 passenger Blown-Flap eSTOL flight profiles.

The flight profiles in Fig. 18 illustrate the changes in aircraft state, denoted as X in the methodology in Fig. 2, and the aerodynamic and propulsion performance. Like the other vehicles, there are differences in the time at which the aircraft reaches cruise altitude, and where changes in aircraft performance occur. The cases with a lower acceleration altitude, h, reach cruise altitude and the end of the departure procedure first. On the takeoff roll, the difference in acceleration rate and the jet velocity are evident, where the 300 ft takeoff has a jet velocity of approximately 20 kts less than that of the maximum power takeoff. The 300 ft takeoff roll uses a 40° flap detent, and a flap change occurs at the acceleration altitude. During the acceleration segment, the aircraft levels out as it accelerates to flaps up velocity. The

200ft takeoff roll also climbs at a lower flight path angle of 7.5° than the 150 ft takeoff roll. In this control strategy, the aircraft is assumed to maintain 80% maximum RPM after the initial takeoff, if neccessary. Thus, it is not able to accelerate up to the cruise velocity of 150 kts, but rather reaches 112 kts by the end of the departure procedure, at 3 nm. The trajectory performance of these cases are summarized in Fig. 19, including a plot for the cumulative total energy over time, and the undertrack noise including both $L_{A,Max}$ and SEL, modeled according to the methodology presented in Section III.E.

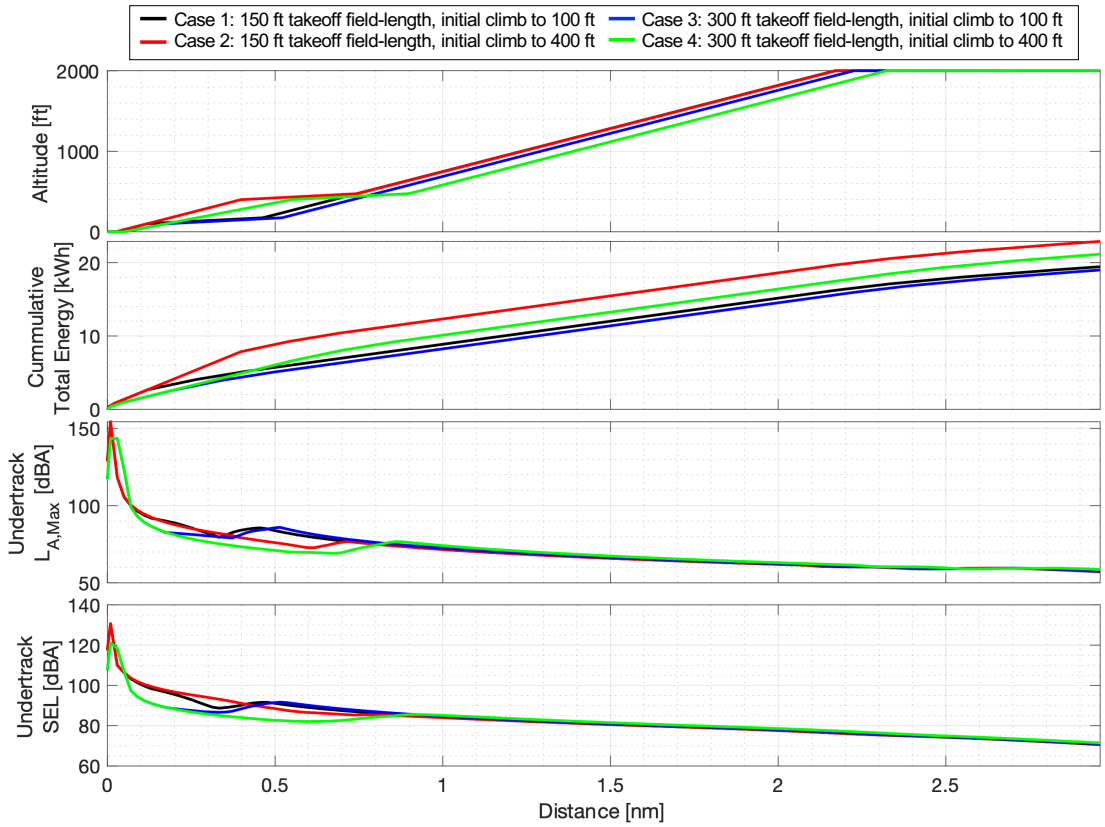

Fig. 19 Trajectory performance results of 6000 lb, 9 passenger Blown-Flap eSTOL case studies.

As presented in Fig. 19 for respective takeoff distances, the lower acceleration altitude, h, results in lower energy consumption during the takeoff procedure. However, when observing the undertrack SEL, Case 1, has a noticeable decrease in noise when compared to the higher acceleration altitude of Case 2. This is assumed to be primarily due to the cutback that occurs at the acceleration altitude. Case 4 displays the lowest undertrack noise early in the flight trajectory as it operates at lower power and gains more altitude than the other cases, however, later in the profile it is at a lower altitude for longer and thus has higher undertrack noise in comparison. Additionally, Case 4 is the slowest procedure and the most energy consuming.

The noise contours for the Blown-Flap eSTOL cases are presented in Fig. 20. At 100% RPM, there is little contour shape and area change with increasing transition altitude as seen in Cases 1 and 2. The contour width tapers off as the vehicle departs. At 65 dB $L_{A,Max}$, climbing to a higher acceleration altitude results in a 0.03 nm^2 reduction in area.

At 80 % RPM the contours in the initial takeoff are noticeably smaller than the 80 % RPM cases. Compared to Case 4, Case 3 widens at a shorter ground-track distance from the origin as the vehicle accelerates. The change in width between Cases 3 and 4, however, is almost equal and both contours taper at a similar rate as the ground-track distance increases. At 65 dB, there is a 0.06 nm^2 decrease in area between Cases 3 and 4.

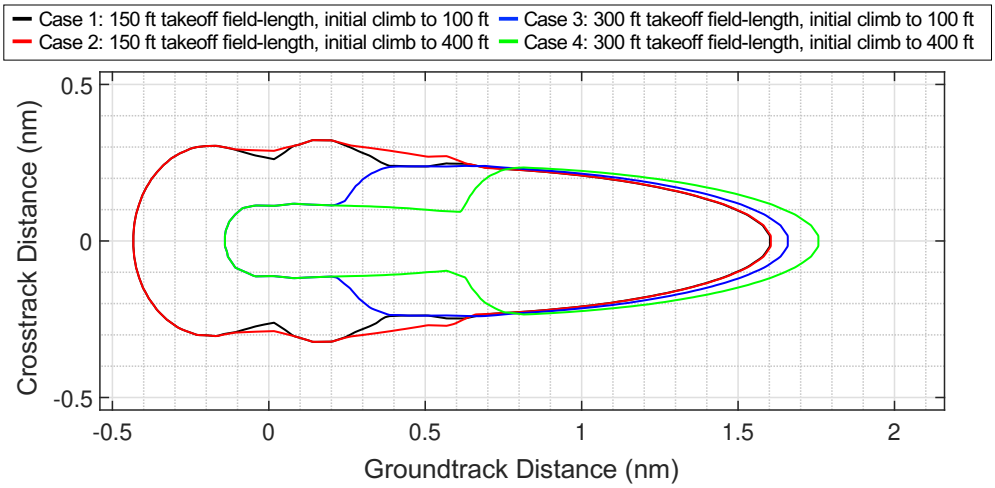

Fig. 20 65 dBA $L_{A,Max}$ single event noise contours for 6000 lb, 9 passenger eSTOL trajectories.

The overall trajectory results are presented in Table 9. The 65 dB $L_{A,Max}$ contour area, total energy, and departure flight duration are summarized. The 300 ft takeoff with the higher acceleration altitude (Case 4) results in the smallest noise contour area. In general, the ability to perform a 300 foot takeoff results in lower RPM and thus overall less community noise impact, and also requires less energy than the respective 150 foot takeoff cases.

Table 9 eSTOL performance results for departure trajectories.

Case Number	Takeoff Field-length (ft)	Acceleration Altitude (ft)	Takeoff RPM	65 dBA $L_{A,Max}$ Noise Contour Area (nm^2)	Total Energy (kWh)	Flight Duration (s)
Case 1	150	100	100%	0.91	19.6	157
Case 2	150	400	100%	0.94	23.0	168
Case 3	300	100	80%	0.63	19.1	162
Case 4	300	400	80%	0.57	21.3	179

V. Conclusion

As Advance Air Mobility continues to mature, it is important to consider the variations of vehicle performance in the development of the AAM airspace. This paper presented a framework for analyzing AAM trajectory design and

modeling of performance and community noise. This enables the assessment of outcomes that result from different operational control strategies for diverse vehicle architectures. While previous work demonstrates efforts of designing AAM vehicles to meet desired mission profiles and quantify the effects of single hemisphere noise propagation, this work demonstrates the development of vehicle specific takeoff trajectories, and how variations in the takeoff control strategy impact the vehicles performance. Additionally, this work demonstrates the ability to model noise specific to the vehicles dynamic state along the trajectory.

A few notable simplifications within the noise model include a uniform inflow assumption that does not consider rotor-wake or rotor-airframe flow interactions. Although constructive-destructive rotor-rotor noise effects were modeled, the noise propagation does not account for noise shielding or reflection from airframe surfaces such as wings or the fuselage. Noise tools capable of modeling these more sophisticated inflows can be readily integrated into the framework to evaluate these additional effects should the level of fidelity be desired.

The vehicles demonstrated in this work are representative to different AAM architectures currently in development in industry. They include a representative 9 passenger Blown-Flap Short Takeoff and Landing vehicle, a 4 passenger Tilt-Rotor Vertical Takeoff and Landing vehicle, and a 2 passenger Lift Plus Cruise Vertical Takeoff and Landing vehicle; however, the methodology is applicable to additional distributed, open-rotor vehicle architectures. The definition of AAM control strategies is closely examined for departure scenarios for regions near airport for different vehicles is presented as case studies in this work. This procedure can be applied to approach procedures and can be used to examine the performance of additional, novel departure procedures.

The results of the departure procedures studied suggest that Tilt-Rotor procedures with a higher vertical takeoff altitude present lower undertrack noise during transition and smaller noise contour area than lower vertical takeoff altitudes, although requiring more energy and time. Similarly, the departure procedures for the Lift plus Cruise eVTOL also present lower undertrack noise for higher vertical takeoff altitudes, but have an additional distinct noise advantage when performing the transition segment while climbing, which does require more energy and time. Both eVTOL vehicles exhibit consistent trends of decreasing noise with increasing energy consumption and flight time across Cases 1 through 4. For the eSTOL vehicle, modulating takeoff field length and RPM settings can reduce the community noise impact. Performing lower power takeoffs reduces the community noise impact but can lead to longer flight durations. These trade-offs amongst various vehicle types highlight considerations for operational sequencing that must be accounted for in future air traffic control strategies for AAM.

Acknowledgments

This work was sponsored by the Federal Aviation Administration (FAA) under ASCENT Center of Excellence Project 84. Opinions, interpretations, conclusions, and recommendations are those of the authors and are not necessarily

endorsed by the United States Government. The authors would like to acknowledge the support of Susumu Shirayama of the FAA Office of Environment and Energy. This work was also sponsored by the The California Resilient and Innovative Mobility Initiative (RIMI). These results are also based upon work supported by the National Science Foundation Graduate Research Fellowship Program under Grant No. DGE-1839285. Any opinions, findings, and conclusions or recommendations expressed in this material are those of the authors and do not necessarily reflect the views of the National Science Foundation.

References

[1] Straubinger, A., Rothfeld, R., Shamiyeh, M., Büchter, K.-D., Kaiser, J., and Plötner, K. O., "An overview of current research and developments in urban air mobility – Setting the scene for UAM introduction," *Journal of Air Transport Management*, Vol. 87, 2020, p. 101852. https://doi.org/https://doi.org/10.1016/j.jairtraman.2020.101852, URL https://www.sciencedirect.com/science/article/pii/S0969699719304302.

[2] "Systems Analysis of Urban Air Mobility Operational Scaling," Ph.D. thesis, Massachusetts Institute of Technology, 2019. URL https://dspace.mit.edu/handle/1721.1/123692.

[3] FAA, "Urban Air Mobility: Concept of Operations v2.0," , 2023. URL https://www.faa.gov/sites/faa.gov/files/Urban%20Air%20Mobility%20%28UAM%29%20Concept%20of%20Operations%202.0_0.pdf.

[4] Vascik, P. D., Balakrishnan, H., and Hansman, R. J., "Assessment of Air Traffic Control for Urban Air Mobility and Unmanned Systems," *8th International Conference on Research in Air Transportation*, 2018. URL https://api.semanticscholar.org/CorpusID:54058339.

[5] Stoll, A. M., Stilson, E. V., Bevirt, J., and Pei, P. P., "Conceptual design of the Joby S2 electric VTOL PAV," *14th AIAA Aviation Technology, Integration, and Operations Conference*, 2014. https://doi.org/10.2514/6.2014-2407.

[6] O'Neill, S., "Electric Air Taxis Create Megadeal Buzz," *Engineering*, Vol. 13, 2022, pp. 5–8. https://doi.org/10.1016/j.eng.2022.04.004.

[7] Dempsey, P., "Aviation Evtol: UP, UP and away!" *Engineering & Technology*, Vol. 16, No. 7, 2021, pp. 26–29. https://doi.org/10.1049/et.2021.0704.

[8] Barbano, M., and Costa, V., "Implementing Urban Air Mobility in a Multi-Level Regulatory Framework: Perspectives from the EU," *2023 International Conference on Unmanned Aircraft Systems (ICUAS)*, IEEE, Warsaw, Poland, 2023, pp. 895–902. https://doi.org/10.1109/ICUAS57906.2023.10156184, URL https://ieeexplore.ieee.org/document/10156184/.

[9] Hartman, D., Hartman, C. L., and Foster, J. V., "Performance Modeling of Urban Air Mobility Vehicles to Support Air Traffic Management Research," *AIAA SCITECH 2023 Forum*, American Institute of Aeronautics and Astronautics, National Harbor, MD & Online, 2023. https://doi.org/10.2514/6.2023-0548, URL https://arc.aiaa.org/doi/10.2514/6.2023-0548.

[10] Onat, E. B., Bulusu, V., Chakrabarty, A., Hansen, M., Sengupta, R., and Sridhar, B., "Evaluating eVTOL Network Performance and Fleet Dynamics through Simulation-Based Analysis," *AIAA SCITECH 2024 Forum*, American Institute of Aeronautics and Astronautics, Orlando, FL, 2024. https://doi.org/10.2514/6.2024-0336, URL https://arc.aiaa.org/doi/10.2514/6.2024-0336.

[11] Ackerman, K. A., Gregory, I. M., Theodorou, E., and Hovakimyan, N., "A Model Predictive Control Approach for In-Flight Acoustic Constraint Compliance," *AIAA Scitech 2021 Forum*, American Institute of Aeronautics and Astronautics, VIRTUAL EVENT, 2021. https://doi.org/10.2514/6.2021-1958, URL https://arc.aiaa.org/doi/10.2514/6.2021-1958.

[12] Ackerman, K. A., and Gregory, I. M., "Comparison of Acoustic Models and Trajectory Generation Methods for an Acoustically-Aware Aircraft," *AIAA SCITECH 2023 Forum*, American Institute of Aeronautics and Astronautics, National Harbor, MD & Online, 2023. https://doi.org/10.2514/6.2023-2543, URL https://arc.aiaa.org/doi/10.2514/6.2023-2543.

[13] Tumuluru Ramesh, N., and V. Pandurangi, P., "A flight performance based optimization model for eVTOL vehicles," preprint, Aug. 2022. https://doi.org/10.31224/2519, URL https://engrxiv.org/preprint/view/2519/version/3669.

[14] Brown, A., and Harris, W., "A Vehicle Design and Optimization Model for On-Demand Aviation," *2018 AIAA/ASCE/AHS/ASC Structures, Structural Dynamics, and Materials Conference*, American Institute of Aeronautics and Astronautics, Kissimmee, Florida, 2018. https://doi.org/10.2514/6.2018-0105, URL https://arc.aiaa.org/doi/10.2514/6.2018-0105.

[15] Clarke, M. A., and Alonso, J., "Evaluating the Performance and Acoustic Footprint of Aircraft for Regional and Urban Air Mobility," *AIAA AVIATION 2021 FORUM*, American Institute of Aeronautics and Astronautics, VIRTUAL EVENT, 2021. https://doi.org/10.2514/6.2021-3205, URL https://arc.aiaa.org/doi/10.2514/6.2021-3205.

[16] Ackerman, K. A., and Gregory, I. M., "Trajectory Generation for Noise-Constrained Autonomous Flight Operations," *AIAA Scitech 2020 Forum*, American Institute of Aeronautics and Astronautics, Orlando, FL, 2020. https://doi.org/10.2514/6.2020-0978, URL https://arc.aiaa.org/doi/10.2514/6.2020-0978.

[17] Johnson, W., "NDARC - NASA Design and Analysis of Rotorcraft," 2015. https://doi.org/NASA/TP-2015-218751, URL https://ntrs.nasa.gov/citations/20150021267, nTRS Author Affiliations: NASA Ames Research Center NTRS Report/Patent Number: ARC-E-DAA-TN22623 NTRS Document ID: 20150021267 NTRS Research Center: Ames Research Center (ARC).

[18] Patterson, M. D., Antcliff, K. R., and Kohlman, L. W., "A Proposed Approach to Studying Urban Air Mobility Missions Including an Initial Exploration of Mission Requirements," *AHS International 74th Annual Forum & Technology Display*, 2018.

[19] Antcliff, K., Whiteside, S., Kohlman, L. W., and Silva, C., "Baseline Assumptions and Future Research Areas for Urban Air Mobility Vehicles," *AIAA Scitech 2019 Forum*, American Institute of Aeronautics and Astronautics, San Diego, California, 2019. https://doi.org/10.2514/6.2019-0528, URL https://arc.aiaa.org/doi/10.2514/6.2019-0528.

[20] Lukaczyk, T. W., Wendorff, A. D., Colonno, M., Economon, T. D., Alonso, J. J., Orra, T. H., and Ilario, C., "SUAVE: An Open-Source Environment for Multi-Fidelity Conceptual Vehicle Design," *16th AIAA/ISSMO Multidisciplinary Analysis and Optimization Conference*, American Institute of Aeronautics and Astronautics, Dallas, TX, 2015. https://doi.org/10.2514/6.2015-3087, URL https://arc.aiaa.org/doi/10.2514/6.2015-3087.

[21] Vegh, J. M., Botero, E., Clarke, M., Smart, J., and Alonso, J., "Current Capabilities and Challenges of NDARC and SUAVE for eVTOL Aircraft Design and Analysis," *AIAA Propulsion and Energy 2019 Forum*, American Institute of Aeronautics and Astronautics, Indianapolis, IN, 2019. https://doi.org/10.2514/6.2019-4505, URL https://arc.aiaa.org/doi/10.2514/6.2019-4505.

[22] Vascik, P. D., and Hansman, R. J., "Constraint Identification in On-Demand Mobility for Aviation through an Exploratory Case Study of Los Angeles," *17th AIAA Aviation Technology, Integration, and Operations Conference*, American Institute of Aeronautics and Astronautics, Denver, Colorado, 2017. https://doi.org/10.2514/6.2017-3083, URL https://arc.aiaa.org/doi/10.2514/6.2017-3083.

[23] Ariza-Montes, A., Quan, W., Radic, A., Koo, B., Kim, J. J., Chua, B.-L., and Han, H., "Understanding the behavioral intention to use urban air autonomous vehicles," *Technological Forecasting and Social Change*, Vol. 191, 2023, p. 122483. https://doi.org/10.1016/j.techfore.2023.122483, URL https://linkinghub.elsevier.com/retrieve/pii/S0040162523001683.

[24] Vascik, P. D., and Hansman, R. J., "Scaling Constraints for Urban Air Mobility Operations: Air Traffic Control, Ground Infrastructure, and Noise," *2018 Aviation Technology, Integration, and Operations Conference*, American Institute of Aeronautics and Astronautics, Atlanta, Georgia, 2018. https://doi.org/10.2514/6.2018-3849, URL https://arc.aiaa.org/doi/10.2514/6.2018-3849.

[25] Cohen, A. P., Shaheen, S. A., and Farrar, E. M., "Urban Air Mobility: History, Ecosystem, Market Potential, and Challenges," *IEEE Transactions on Intelligent Transportation Systems*, Vol. 22, No. 9, 2021, pp. 6074–6087. https://doi.org/10.1109/TITS.2021.3082767, URL https://ieeexplore.ieee.org/document/9447255/.

[26] Vascik, P. D., "Systems Analysis of Urban Air Mobility Operational Scaling," Ph.D. thesis, 2019.

[27] Afonso, F., Ferreira, A., Ribeiro, I., Lau, F., and Suleman, A., "On the design of environmentally sustainable aircraft for urban air mobility," *Transportation Research Part D: Transport and Environment*, Vol. 91, 2021, p. 102688. https://doi.org/10.1016/j.trd.2020.102688, URL https://linkinghub.elsevier.com/retrieve/pii/S1361920920308725.

[28] Thomas, Jacqueline, "Systems Analysis of Community Noise Impacts of Advanced Flight Procedures for Conventional and Hybrid Electric Aircraft," PhD Dissertation, Massachusetts Institute of Technology, Cambridge, MA, 2020. URL https://dspace.mit.edu/handle/1721.1/125995.

[29] Ko, J., and German, R. J., Brian J., "Community Noise Impact of Multirotor Configurations During Landing Procedures," *AIAA AVIATION 2023 Forum*, 2023. https://doi.org/10.2514/6.2023-3362.

[30] Li, S. K., and Lee, S., "Prediction of Urban Air Mobility Multirotor VTOL Broadband Noise Using UCD-QuietFly," *JOURNAL OF THE AMERICAN HELICOPTER SOCIETY*, Vol. 66, 2021. https://doi.org/DOI:10.4050/JAHS.66.032004.

[31] Li, S. K., and Lee, S., "Prediction of Rotorcraft Broadband Trailing-Edge Noise and Parameter Sensitivity Study," *Journal of the American Helicopter Society*, Vol. 65, 2020. https://doi.org/10.4050/JAHS.65.042006.

[32] NASA Ames Research Center, Silva, C., and Johnson, W., "Practical Conceptual Design of Quieter Urban VTOL Aircraft," *Proceedings of the Vertical Flight Society 77th Annual Forum*, The Vertical Flight Society, Virtual Conference, 2021, pp. 1–21. https://doi.org/10.4050/F-0077-2021-16739, URL https://vtol.org/store/product/practical-conceptual-design-of-quieter-urban-vtol-aircraft-16739.cfm.

[33] Rizzi, S. A., Letica, S. J., Boyd, D. D. J., and Lopes, L., "Prediction of Noise-Power-Distance Data for Urban Air Mobility Vehicles," *JOURNAL OF AIRCRAFT*, Vol. 61, No. 1, 2024, pp. 166–182. https://doi.org/10.2514/1.C037435, URL https://arc.aiaa.org/doi/10.2514/1.C037435.

[34] Rizzi, S. A., and et. al., "Urban Air Mobility Noise: Current Practice, Gaps, and Recommendations," NASA TP–2020-5007433, 2020.

[35] Rizzi, S., Page, J. A., and Rui, C., "Comparison of two community noise models applied to a NASA urban air mobility concept vehicle," *50th International Congress and Exposition on Noise Control Engineering (Inter-Noise 2021)*, Institute of Noise Control Engineering (I-INCE), 2021. URL https://ntrs.nasa.gov/citations/20210015134.

[36] Yeung, N., la Cruz, J. D., Pellerito, V. R., Wang, Z., Lepe, M., Huynh, J. L., and Hansman, R. J., "Flight Procedure and Community Noise Modeling of Advanced Air Mobility Flight Vehicles," *AIAA AVIATION 2023 Forum*, ???? https://doi.org/10.2514/6.2023-3361, URL https://arc.aiaa.org/doi/abs/10.2514/6.2023-3361.

[37] De La Cruz, J. J., "Methodology to Model Aircraft and Propulsor Performance of Advanced Air Mobility," Master's thesis, University of California, Irvine, 2023. URL https://escholarship.org/uc/item/6tk8v3r6.

[38] Drela, M., and Youngren, H., "XROTOR User Guide," Massachusetts Institute of Technology, Cambridge, MA, 2003, URL https://web.mit.edu/drela/Public/web/xrotor/xrotor_doc.txt.

[39] Lopes, L. V., and Burley, C. L., "ANOPP2 User's Manual: Version 1.2," NASA TM 2016-219342, 2016.

[40] Krishnamurthy, S., Tuttle, B. C., and Rizzi, S., "A Synthesis Plug-in for Steady and Unsteady Loading and Thickness Noise Auralization," AIAA Aviation 2020 Forum, 2020. https://doi.org/10.2514/6.2020-2597.

[41] Fink, M., "Airframe Noise Prediction Method," Tech. Rep. FAA-FRD-77-29, 1977.

[42] Guo, Y., "An Improved Landing Gear Noise Prediction Scheme," Tech. Rep. NASA/CR-NAS1-NNL04AA11B, The Boeing Company, Huntington Beach, CA, 2006.

[43] Guo, Y., "Aircraft Flap Side Edge Noise Modeling and Prediction," *17th AIAA/CEAS Aeroacoustics Conference (32nd AIAA Aeroacoustics Conference)*, The Boeing Company, Portland, OR, 2011. https://doi.org/10.2514/6.2011-2731.

[44] Farassat, F., "Derivation of Formulations 1 and 1A of Farassat," Tech. Rep. TM-2007-214853, Langley Research Center, 10 2007.

[45] Brooks, T. F., Pope, D. S., and Marcolini, M. A., "Airfoil Self-Noise and Prediction," Tech. Rep. NASA-RP-1218, Hampton, Virginia, 1989.

[46] Yeung, N., Pellerito, V. R., la Cruz, J. D., Emmanouilidi, M., and Huynh, J. L., "Component-Based Noise Modeling for Distributed Propulsion Blown-Flap STOL Vehicle Flight Procedures," *AIAA AVIATION 2022 Forum*, 2022. https://doi.org/10.2514/6.2022-3508.

[47] Vesa, J., "Design of an Anechoic Chamber for Aeroacoustic Testing and Analysis of Large UAS Propellers," Master's thesis, Mississippi State University Masters Thesis, 2020. URL https://scholarsjunction.msstate.edu/td/1307.

[48] "Standard Values of Atmospheric Absorption as a Function of Temperature and Humidity. SAE ARP866A," Tech. rep., Prepared by SAE Committee A-21, 1975.

[49] Pascioni, K. A., Watts, M. E., Houston, M., Lind, A., Stephenson, J. H., and Bain, J., "Acoustic Flight Test of the Joby Aviation Advanced Air Mobility Prototype Vehicle," *28th AIAA/CEAS Aeroacoustics 2022 Conference*, Southampton, UK, 2022. https://doi.org/10.2514/6.2022-3036.

[50] Stoll, A. M., and Milkic, G. V., "Transition Performance Of Tilt Propeller Aircraft," Tech. rep., 2022. URL https://doi.org/10.4050/F-0078-2022-17443.

[51] Jha, A., Prabhakar, N., Karbowski, D., and German, B., "Urban Air Mobility: A preliminary case study for Chicago and Atlanta," *2022 IEEE Transportation Electrification Conference Expo (ITEC)*, 2022, pp. 300–306. https://doi.org/10.1109/ITEC53557.2022.9814052.

[52] Joby, "Joby Confirms Revolutionary Low Noise Footprint Following NASA Testing," , 2022. URL https://www.jobyaviation.com/news/joby-revolutionary-low-noise-footprint-nasa-testing/.

[53] Pascioni, K. A., Watts, M. E., Houston, M. L., Lind, A. H., Stephenson, J. H., and Bain, J. J., "Acoustic Flight Test of the Joby Aviation Advanced Air Mobility Prototype Vehicle," *Aeroacoustics 2022*, NASA Langley Research Center and Joby Aviation, Hampton, VA, USA, 2022. Presented at the Aeroacoustics 2022 Conference, NASA/Joby collaboration as part of the AAM National Campaign Developmental Test (NC-DT).

[54] Bacchini, A., and Cestino, E., "Electric VTOL Configurations Comparison," *Aerospace*, Vol. 6, No. 3, 2019. https://doi.org/10.3390/aerospace6030026.

[55] Agrawal, D., Asad, F., Berk, B. M., Long, T., Lubin, J., Courtin, C., Drela, M., Hansman, R. J., and Thomas, J. L., "Wind Tunnel Testing of a Blown Flap Wing," *AIAA Aviation 2019 Forum*, 2019. https://doi.org/10.2514/6.2019-3170.

[56] Courtin, C., Mahseredjian, A., Dewald, A. J., Drela, M., and Hansman, J., *A Performance Comparison of eSTOL and eVTOL Aircraft*, 2021. https://doi.org/10.2514/6.2021-3220.

[57] Courtin, C., Hansman, R. J., and Drela, M., *Flight Test Results of a Subscale Super-STOL Aircraft*, 2020. https://doi.org/10.2514/6.2020-0977.